



UNIVERSITY OF LEEDS

This is a repository copy of *Experimental investigation of wire arc additively manufactured steel T-stub connections*.

White Rose Research Online URL for this paper:

<https://eprints.whiterose.ac.uk/208238/>

Version: Accepted Version

Article:

Guo, X., Kyvelou, P., Ye, J. orcid.org/0000-0002-6857-7450 et al. (1 more author) (2023) Experimental investigation of wire arc additively manufactured steel T-stub connections. *Journal of Constructional Steel Research*, 211. 108106. ISSN 0143-974X

<https://doi.org/10.1016/j.jcsr.2023.108106>

© 2023 Published by Elsevier Ltd. This is an author produced version of an article published in *Journal of Constructional Steel Research*. Uploaded in accordance with the publisher's self-archiving policy. This manuscript version is made available under the CC-BY-NC-ND 4.0 license <http://creativecommons.org/licenses/by-nc-nd/4.0/>

Reuse

This article is distributed under the terms of the Creative Commons Attribution-NonCommercial-NoDerivs (CC BY-NC-ND) licence. This licence only allows you to download this work and share it with others as long as you credit the authors, but you can't change the article in any way or use it commercially. More information and the full terms of the licence here: <https://creativecommons.org/licenses/>

Takedown

If you consider content in White Rose Research Online to be in breach of UK law, please notify us by emailing eprints@whiterose.ac.uk including the URL of the record and the reason for the withdrawal request.



eprints@whiterose.ac.uk
<https://eprints.whiterose.ac.uk/>

Experimental investigation of wire arc additively manufactured steel

T-stub connections

Xi Guo*, Pinelopi Kyvelou, Jun Ye, Leroy Gardner

Department of Civil and Environmental Engineering, Imperial College London, London SW7

2AZ, UK

Abstract: This paper presents an experimental investigation into the structural response of wire arc additively manufactured (WAAM) steel T-stub connections subjected to tension. A total of eighty T-stub specimens featuring different printing strategies, bolt arrangements and geometric configurations were tested to failure. 3D laser scanning was employed to determine the specimen geometry, while digital image correlation (DIC) was used to monitor the strain and displacement fields during testing. Utilising the DIC data, a new method was introduced for the determination of the failure mode and key points on the load-deformation response of T-stub connections. The structural response of the WAAM T-stubs generally followed the anticipated trends, though the geometric irregularities resulted in a delay in the development of prying action in some specimens and the printing strategy was shown to have a clear influence on the load-carrying capacity. Finally, comparisons between the test results and the capacity predictions yielded by existing design equations were made; overall, reasonable agreement was achieved, but further research is required to establish reliable design rules that are specific to this form of manufacture.

Key words: 3D printing; bolted connections; plastic hinge; prying action; plastic moment; T-stub; wire arc additive manufacturing

1. Introduction

Recent research has shown that wire arc additive manufacturing (WAAM) has the potential to bring enhanced automation and sustainability to the construction industry [1-5]. In particular, used in conjunction with topology optimisation, WAAM can be employed to build structural components in a time, cost and material-efficient manner, with reduced wastage [6-12]. Meanwhile, with almost no geometrical restrictions, WAAM lends itself to the production of structural joints, for which complex shapes are often needed [13-17]. However, for the wider integration of this technology into the construction industry, fundamental underpinning experimental data and design guidelines are required.

The present study focusses on WAAM connections, specifically T-stubs. Connections play a crucial role in the behaviour of steel structures, and their design and fabrication are often complex and costly [18]. T-stubs in tension have been extensively tested in the past because their behaviour represents the response of the key components in a wide range of structural steel joints [19-23]. According to Eurocode 3 Part 1.8 [24], T-stubs can exhibit three distinct failure modes: Mode 1 occurs for T-stubs comprising strong bolts and weak flanges, with four plastic hinges developing in the flange outstands – two next to the web-to-flange junction and two near the bolts – see Figure 1(a). Mode 2, shown in Figure 1(b), involves failure of the bolts and the formation of two plastic hinges at the web-to-flange junction.

Mode 3, which occurs for T-stubs with strong flanges and weak bolts, is characterised by bolt failure alone – see Figure 1(c). Substantial research has been carried out on T-stubs of different material types, including high strength steel, stainless steel and aluminium alloy [25-28], and different geometries [29-34], while the influence of the prying action that develops in the flanges during loading [35-40], as well as that of the bolt preload and membrane action [41-48] on the structural response, has been extensively investigated.

In addition to T-stubs with two bolts in a row (i.e. one bolt per flange outstand – see Figure 1), which constitute the most commonly employed type of T-stub connection, T-stubs with four bolts in a row (i.e. two bolts per flange outstand), which are not covered in Eurocode 3, have also been receiving increasing attention [49,50]. According to Demonceau et al. [49], essentially the same three failure modes described above can also arise in T-stubs with four bolts in a row – see Figure 2.

In order to investigate the structural response of WAAM steel T-stubs, experiments on 52 WAAM T-stubs with two bolts in a row and 28 WAAM T-stubs with four bolts in a row, have been conducted and are presented in this paper. Advanced experimental techniques, featuring 3D laser scanning and digital image correlation (DIC), have been used to create three-dimensional models of all specimens and to monitor the deformations that developed during testing, respectively. The test results are compared against the design predictions of Eurocode 3 Part 1.8, as well as against the predictions yielded by a method proposed in [49,50] for T-stubs with four bolts in a row. The key findings are presented and discussed.

2. Manufacturing and T-stub specimen geometry

All specimens were manufactured by the Dutch company MX3D [51], using their multi-axis robotic WAAM technology [51]. The welding wire used for the fabrication of all specimens was ER70S-6 (EN ISO 14341-A G 42 4 M21 3Si1) [52], the chemical composition and mechanical properties of which are given in Tables 1 and 2 respectively. All specimens were printed on a 300×300×20 mm S235 steel base plate. The adopted printing parameters are reported in Table 3. Figure 3 illustrates the different printing strategies that were employed for the examined specimens. Some specimens were printed continuously, as shown in Figures 3(a) and (b), while others were printed in two stages, with the flange printed first and the web printed second, directly on the flange – see Figures 3(c) and (d). Finally, specimens with both sharp and rounded corners were manufactured – see Figure 3.

All T-stubs were first sandblasted to remove any slag or soot from the welding process and then laser scanned using a FARO Design ScanArm 2.0 laser scanner, with a scan rate of 600,000 points/second and an accuracy of 0.075 mm [53]. The digital models of all specimens were processed in the software Geomagic Wrap [54] and then exported as STL files for the determination of their geometric properties.

The examined specimens were of two different geometric configurations; these are shown in Figure 4, where t is the thickness of the flanges, d_0 is the bolt hole diameter, m is the distance between the web-to-flange junction and the bolt line (defined as the line across the bolt hole centres parallel to the web), b is the length of the flange parallel to the web and a is the corner

radius or length of the transition between the web and flange outstand for the continuously and individually printed specimens with rounded (or stepped) corners respectively. For the T-stubs with two bolts, e is the distance between the centre of the bolt hole and the tip of the flange, while for the T-stubs with four bolts in a row, e_1 is the distance between the centres of the two bolt holes and e_2 is the distance from the centre of the outer bolt hole to the tip of the flange. Finally, the length of the transition between the web and the flange is denoted as a for the specimens with rounded corners – see Figures 4(a) and (b).

The adopted specimen labelling system starts with “T1” or “T2” for the T-stubs with one or two bolts per flange outstand respectively, followed by the length of the flange parallel to the web b in mm, the non-dimensional ratio λ ($\lambda = e/(m+a)$ for T-stubs with two bolts and $\lambda = (e_1+e_2)/(m+a)$ for T-stubs with four bolts in a row), the letter “C” or “I” for the T-stubs with their flanges and web printed continuously or individually respectively – see Figure 3, and, finally, the letter “R” or “S” for the T-stubs with rounded or sharp corners respectively. For example, Specimen T1-40-0.67-C-R is a continuously printed T-stub with rounded corners, one bolt per flange outstand (i.e. 2 in total), a flange length of 40 mm and a λ ratio of 0.67.

The dimensions of all specimens were measured using Vernier callipers and radius gauges, while the average thickness of the flanges, which, due to the surface undulations of the WAAM surface, could not be effectively measured using conventional tools, were determined in Rhino 3D [55] using the laser scan data, as described in [7]. A summary of the

dimensions of the T-stubs are presented in Tables 4 and 5 for the specimens with two and four bolts in a row, respectively.

3. Test setup

All specimens were tested in pairs, with each WAAM T-stub connected to a grade S700 high-strength steel (HSS) T-stub, by means of hand-tightened (i.e. essentially zero pre-stress) M12 bolts with bolt hole clearances of 2 mm. The bolt grades, which were either 8.8 or 10.9 depending on the specimen, were selected to prevent bolt failure (i.e. Mode 3 failure). A digital image correlation (DIC) system with two pairs of cameras was employed to capture the strain fields during testing, with each camera pair monitoring the upper surface of each flange outstand. Two Linear Variable Differential Transformers (LVDTs) were also installed on the two sides of each T-stub to monitor the displacements parallel to the T-stub webs. All tests were carried out using a 250 kN Instron testing machine. The tensile load was applied using displacement control at a constant rate of 0.8 mm/min, resulting in failure of the specimens within 30 minutes. An overview of the test setup is presented in Figure 5.

4. Test results

4.1. *Load-displacement curves*

The load-displacement curves of conventionally manufactured T-stubs typically feature two stages – an elastic stage and a plastic stage, with the latter generally exhibiting a plateau followed by strain hardening; the transition point between the two stages defines the yield

load of the T-stub i.e. the plastic resistance of the connection [31,43,44]. In some cases, a third stage, featuring a re-rise in stiffness after large deformations and referred as the “second hardening branch” [47] occurs; this is caused by the development of membrane action in the flange outstands and bearing between the bolt shank and bolt hole [25,27,47].

The load-displacement curves for the WAAM T-stubs tested herein are presented in Figures 6 and 7 for the T-stubs with two bolts and four bolts per flange outstand respectively, with the displacement measured on the T-stub web, 30 mm away from the web-to-flange junction.

While two-stage and three-stage load-displacement curves were typical – see Figures 8(a) and (b), curves with additional ‘kinks’ were also evident. Preliminary FE simulations, conducted in Abaqus [58], indicated that the additional kinks occurred due to gaps between the upper and lower T-stub flanges, caused by surface undulations inherent to the WAAM process or bowing of the WAAM T-stub flange – see Figure 9. As shown in Figure 10, increasing the gap size between the T-stub flanges in the FE simulations resulted in an increasingly prominent additional kink in the load-displacement curve. The existence of these initial gaps between the T-stub flanges caused a delay in the development of prying forces, the importance of which has been widely recognised [32-37]. Once contact between the flanges had been established, prying forces developed, and an increase in stiffness was observed. Determination of the point of this contact was thus considered to be significant.

To determine the point of contact between the flanges in the experiments, the displacement at the tips of the flanges of the WAAM T-stubs was monitored by means of a virtual

displacement gauge (VDG_E) through the DIC system, as illustrated in Figure 11. In Figure 12, the load is plotted against the vertical displacement at the flange tip of a typical specimen, where three stages of behaviour can be observed. In the first stage, the flange rises as the bolt elongates with increasing load, with both the web-to-flange junction and the bolt remaining elastic, until a load level corresponding to yielding at the web-to-flange junction is reached. The second stage is then triggered, characterised by the descent of the flange arising owing to the reduced rotational stiffness following the formation of the plastic hinge at the web-to-flange junction. Finally, in third stage, the descent of the WAAM flange tip is halted as it comes into contact with the flange below, resulting in decreasing displacement with increasing load. A simplified model of the load-vertical displacement curve of the flange tip is also illustrated in Figure 12. Hence, the transition from the first to the second stage indicates yielding in the web-to-flange junction, and from the second to the third stage, contact between the upper and lower flanges.

4.2. Determination of plastic hinges in the flanges and yielding of bolts

In order to gain a comprehensive understanding of the response of WAAM T-stub connections, a detailed investigation of the development of the plastic hinges in the flanges and yielding of the bolts is required; this is addressed in this section.

Typically, the failure modes of T-stubs have been identified either based on observations of the deformed shape of the flanges, which can be subjective, or by monitoring the strains at critical locations during testing, but often without clear criteria for defining failure modes

having been established [26-28]. In this section, a consistent method to identify the development of the plastic hinges is proposed, whereby the bending moments arising through the thickness of the flanges at critical locations (i.e. at the web-to-flange junction and at the bolt line) are estimated based on the measured strains from virtual strain gauges (VSG), and compared against the theoretical plastic moment resistance of the flanges. Meanwhile, a criterion for the definition of bolt yielding based on the load-elongation response of the bolts is introduced. Note that the mechanical properties of the WAAM T-stubs were taken from [13], where tensile tests on WAAM coupons, manufactured using the same feedstock material and printing parameters as the T-stubs tested herein, were conducted – see Table 6.

The first step of the proposed method is to extract the normal strains in the transverse (y) direction ε_{yy} from the DIC data, at the critical locations illustrated in Figures 11(a) and (b) for the T-stubs with 2 bolts and 4 bolts in a row respectively. Two typical load-strain responses are presented in Figure 13, where the positive strains at the web-to-flange junction (USG_C) indicate tensile deformation on the exposed surface, while negative strains at the bolt line indicate compressive deformation on the exposed surface. Note that the strain at the bolt line is taken as the average of the strains measured on both sides of the bolt hole (VSG_{BL1} and VSG_{BL2}) – see Figure 11. Subsequently, the stress distribution across the thickness can be obtained at all load levels based on the average stress-strain curve of the material [13], assuming a linear strain distribution through the flange thickness, with the maximum strain at the extreme fibre being equal to the DIC strain ε_{yy} – see Figure 14(a).

Based on the acquired stress distribution, the corresponding bending moment M_x was obtained by discretising the flange thickness into n layers of height δt (taken equal to 0.01 mm) and performing numerical integration thus:

$$M_x = \sum_1^n z_i \sigma_i l_{\text{eff}} \delta t \quad (1)$$

where l_{eff} is the effective length of the plastic hinge determined according to Eurocode 3 [24], z_i is the distance of layer i from the neutral axis of the flange and σ_i is the stress determined from the stress-strain curve of the WAAM material at layer i , for a value of ε_i equal to:

$$\varepsilon_i = \left(\frac{z_i}{t/2} \right) \varepsilon_{yy} \quad (2)$$

where ε_i is the strain in each cross-sectional layer.

The strain required for the formation of a plastic hinge can be chosen by comparing the bending moment M_x obtained by Equation (1) against the theoretical plastic moment M_{pl} calculated by Equation (3):

$$M_{\text{pl}} = \frac{l_{\text{eff}} t^2 f_y}{4} \quad (3)$$

For the examined specimens, M_x was found to reach 98% of the theoretical plastic moment M_{pl} at a strain of $5\varepsilon_y$, where ε_y is the yield strain taken as $f_y/E = 0.0014$, and f_y and E are the yield stress and Young's modulus – see Table 7. The $5\varepsilon_y$ threshold is shown in Figure 15,

where, for a typical specimen, the bending moment M_x is plotted against the surface strain ε_{yy} at the web-to-flange junction and the bolt line. When the surface strain ε_{yy} reaches $5\varepsilon_y$, the section can be considered to be essentially fully plastic, with the corresponding load applied to the T-stub being the yield load of the section. Based on this criterion, the yield loads for yielding at the web-to-flange conjunction $F_{y,C}$ and at the bolt line $F_{y,BL}$ for the T-stubs with two bolts and four bolts in a row are summarised in Tables 8 and 9, respectively.

Regarding the point at which yielding of the bolt occurs, this can be determined by monitoring the bolt elongation (of the inner bolt for T-stubs with four bolts in a row), measured by means of a virtual displacement gauge (provided by the DIC system) positioned at the top of the bolt head, as illustrated in Figure 11. Bolt yielding was identified as the point on the load-elongation curve where a marked drop in stiffness occurs; the corresponding load is denoted $F_{y,B}$. The loads corresponding to yielding of the bolts $F_{y,B}$ for the examined T-stubs with two bolts and four bolts in a row are summarised in Tables 8 and 9, respectively.

4.3. Determination of plastic resistance and identification of failure mode

The load-displacement curves of four typical T-stub specimens are plotted in Figure 16, where the different stages of the behaviour and key points, namely the yield points of the web-to-flange junction, bolt line and bolt and when the upper and lower flange outstands (left and right) come in contact, are marked. Following the development of yielding at two of the three key locations, a pronounced drop in stiffness can be observed, corresponding to the

formation of a plastic mechanism in the T-stub, after which complete failure eventually occurs. The load corresponding to the occurrence of yielding at the second location is therefore defined as the collapse load $F_{\text{coll,test}}$ of the T-stub. Note that if yielding at the web-to-flange conjunction develops prior to the establishment of contact between the upper and lower flanges, a plastic mechanism is formed, accompanied by a loss in stiffness, up until the point that the two flanges come into contact, after which a recovery in stiffness takes place.

The failure mode of the T-stub can be identified based on the location of the second point of yielding. According to Eurocode 3 Part 1.8 [24] and the literature [49], Mode 1 involves the formation of plastic hinges at the web-to-flange junction and at the bolt line (the inner bolt line for the T-stubs with four bolts in a row), while for Mode 2, plasticity develops at the web-to-flange junction and in the bolt. Thus, since yielding at the web-to-flange junction was always found to precede either yielding of the bolt or of the flange at the bolt line, the collapse load $F_{\text{coll,test}}$ of the specimens failing in Mode 1 was equal to the load at which yielding of the bolt line $F_{y,BL}$ occurred, while that of specimens failing in Mode 2 was equal to the bolt yield load $F_{y,B}$. The collapse loads and failure modes of the T-stubs with two bolts and four bolts in a row examined herein are summarised in Tables 8 and 9, respectively.

Typical deformed specimens, grouped by failure mode, are presented in Figure 17, where it can be observed that identification of the failure mode by inspection would have been challenging. Conversely, the proposed approach provides a consistent and accurate way to determine both the collapse loads and failure modes.

In certain cases, the load applied to the T-stubs was found to keep rising even after the collapse load had been attained, and even after yielding had occurred at three locations – see Figure 16(d). This additional capacity is attributed to strain hardening of the material and the development of membrane action in the flanges, with contact between the bolt shank and the bolt hole [47]. The eventual ultimate loads $F_{u,\text{test}}$, including this additional capacity, obtained for the T-stubs with 2 bolts and with 4 bolts in a row are presented in Tables 8 and 9, respectively. It is worth noting that the ultimate loads $F_{u,\text{test}}$ obtained in the current test programme were governed by ultimate (inner) tensile bolt failure for most specimens – see Figure 18(a), while shear-out and punching failure (i.e. the bolt head punching through the flange) were also observed for two specimens – see Figures 18(a) and (b), respectively.

5. Influence of printing strategy

The loads corresponding to yielding at the web-to-flange junction $F_{y,C}$, bolt line $F_{y,BL}$ and bolt $F_{y,B}$, as well as plastic collapse $F_{\text{coll},\text{test}}$, taken as the lower value of $F_{y,BL}$ and $F_{y,B}$ (see Section 4.2), obtained from the test results are used in this section to evaluate the influence of the different printing strategies on the structural performance of the examined T-stub connections. The specimens with rounded corners that were continuously printed, labelled C-R, were chosen as the benchmark against which the other specimens were compared. Furthermore, in order to eliminate the influence of the geometrical variability between specimens, the aforementioned loads were normalised by the thickness t and width b of each flange. The

mean and COV values of the comparative load ratios, grouped by printing strategy, are presented in Table 10.

The plastic resistances $F_{\text{coll, test}}$ of the T-stubs with rounded corners were found to be higher than those with sharp corners, due to the length of the lever between the bolt hole and the web-to-flange conjunction (i.e. the distance between the two plastic hinges, marked as m in Figure 4) being reduced because of the gradual flange-to-web transition. Furthermore, the T-stubs printed in two steps (first the flange and then the web) exhibited higher plastic resistances than the continuously printed ones, regardless of the type of corner. Overall, the I-R type specimens exhibited the strongest performance, with their plastic resistances being up to 15% higher than the weakest specimen type (i.e. C-S type).

Similarly, given that the loads corresponding to the formation of plastic hinges at the web-to-flange junctions and at the bolt lines are closely related to the distance m , the highest values of $F_{y,C}$ and $F_{y,BL}$ were attained by the specimens with rounded corners. Furthermore, the bolt line yield loads $F_{y,BL}$ were higher for the specimens printed in two steps (rather than continuously), with the values of $F_{y,BL}$ for the I-R type specimens being 18% higher on average than the C-R type specimens, and for the I-S type specimens being 8% higher on average than the C-S type specimens.

The yield loads at the web-to-flange junction $F_{y,C}$ of the I-R type specimens were found to be 7% lower on average than the C-R type specimens. This is attributed to the more pronounced

flange bowing that arose in the specimens printed in two steps, leading to a delay in the development of prying action and, thus, to premature yielding at the conjunction.

Finally, the loads corresponding to bolt yield $F_{y,B}$ of the I-R type specimens were noticeably higher (about 7% on average) than of all other specimens, while almost similar bolt yield loads were obtained for the C-R, C-S and I-S type specimens. This is attributed to the higher levels of bending that developed as a result of the flange rotation for all specimen types apart from the I-R type, where the least rotation arose due to the high rotational stiffness of the conjunction, leading to the bolt being mainly subjected to tension.

6. Design equations

Design equations for T-stubs with two bolts in a row are provided in Eurocode 3 Part 1.8 [24], along with the definition of the effective length, which depends on the yield line mechanism that develops in the T-stub flange. For T-stubs with four bolts in a row, design equations have been provided by Demonceau et al. in [49], while the recommended effective length can be found in [50].

6.1. Yield line pattern and effective length

According to Eurocode 3 Part 1-8 [24], three main types of yield line pattern can occur in T-stub flanges, namely beam, circular and non-circular patterns – see Figure 19. The effective length of the yield line depends on the considered pattern and can be calculated as a function of the geometrical properties. For T-stubs with two bolts in a row, the effective length l_{eff} of

the beam, non-circular and circular patterns are given by Equations (4), (5) and (6) respectively.

$$l_{\text{eff,bp}} = b \quad (4)$$

$$l_{\text{eff,np}} = 4m + 1.25n \quad (5)$$

$$l_{\text{eff,cp}} = \min(2\pi m; \pi m + 2e) \quad (6)$$

where

$$n = \min(e; 1.25m) \quad (7)$$

The subscripts bp , np and cp denote the beam, non-circular and circular yield line mechanisms, respectively, and n is the distance between the bolt hole centre and the position of the prying force (which is normally at the flange tip), but with $n < 1.25m$. Yielding in a beam or non-circular yield pattern usually indicates a Mode 1 or 2 failure, while a circular yield line pattern can only be observed in Mode 1 failure. Thus:

$$l_{\text{eff,1}} = \min(l_{\text{eff,bp}}; l_{\text{eff,np}}; l_{\text{eff,cp}}) \quad (8)$$

$$l_{\text{eff,2}} = \min(l_{\text{eff,bp}}; l_{\text{eff,np}}) \quad (9)$$

where $l_{\text{eff,1}}$ and $l_{\text{eff,2}}$ are the effective lengths that can potentially cause Mode 1 or 2 failure, respectively.

In [50], it was concluded that Equations (4) and (6) remain applicable to T-stubs with four bolts in a row, while Equation (5) can only be used for the determination of the effective length corresponding to Mode 1. For Mode 2, the effective length for non-circular patterns is given by:

$$l_{\text{eff,np}} = 5.685m + 5.867n \quad (10)$$

in which

$$n = \min(e_1 + e_2; 1.25m) \quad (11)$$

6.2. Plastic collapse load predictions

In line with [24], for T-stubs with two bolts in a row, the design plastic resistances F_{Rd} for the three modes illustrated in Figure 1 are defined as:

$$\text{Mode 1:} \quad F_{\text{Rd},1} = \frac{(8n - 2e_w)M_{\text{pl},1}}{2mn - e_w(m + n)} \quad (12)$$

$$\text{Mode 2:} \quad F_{\text{Rd},2} = \frac{2M_{\text{pl},2} + n \sum F_{\text{T,Rd}}}{m + n} \quad (13)$$

$$\text{Mode 3:} \quad F_{\text{Rd},3} = \sum F_{\text{T,Rd}} \quad (14)$$

in which

$$e_w = \frac{d_w}{4} \quad (15)$$

where $M_{\text{pl},1}$ and $M_{\text{pl},2}$ can be calculated by Equation (3) using $L_{\text{eff},1}$ and $L_{\text{eff},2}$, respectively, $\sum F_{\text{T,Rd}}$ is the design resistance of all of the bolts in tension and d_w is the diameter of the bolt head.

Additionally, for the special case where no prying forces develop, the design resistance $F_{\text{Rd,np}}$ can be calculated using Equation (16):

$$F_{\text{Rd},2} = \frac{2M_{\text{pl},1}}{m} \quad (16)$$

For T-stubs with four bolts in a row, Equation (12), which should be used in conjunction with Equation (11), remains applicable for Mode 1, since the location of the plastic hinges is essentially unchanged – see Figure 2(a). Similarly, Equation (14) can be used for Mode 3, with a reduction factor of 0.9.

Finally, the equation accounting for the contribution of the outer bolts for Mode 2 is:

$$F_{Rd,2} = \frac{2M_{pl,2} + \sum F_{T,Rd} \left(\frac{n_1^2 + 2n_2^2 + 2n_1n_2}{n_1 + n_2} \right)}{m + n_1 + n_2} \quad (17)$$

where $n_1 = e_1$ and $n_2 = e_2$ with $n_2 \leq 1.25m + n_1$.

7. Comparisons between test results and design equations

Comparisons are now made between the test results and the plastic resistance predictions determined using the equations introduced in Section 6, based on the measured geometric and material properties. The obtained test-to-prediction resistance ratios are presented in Tables 8 and 9 for the T-stubs with two bolts and four bolts in a row, respectively. Note that since the design plastic resistances for Mode 1 ($F_{Rd,1}$) and Mode 2 ($F_{Rd,2}$) correspond to yielding at the bolt line and in the bolt respectively, the value of $F_{Rd,1}$, obtained from Equation (12), are compared against $F_{y,BL}$ (see Section 4.2), while $F_{Rd,2}$, calculated using Equations (13) or (17) for the T-stubs with two bolts or four bolts in a row, respectively, are compared against $F_{y,B}$ (see Section 4.2). Meanwhile, the design resistance $F_{Rd,np}$, obtained from Equation (16), is evaluated against $F_{y,C}$ (corresponding to yielding at the web-to-flange conjunctions – see Section 4.2), due to the absence of prying forces at the early stages of loading.

7.1. *T-stubs with two bolts in a row*

The plastic resistances associated with yielding at the bolt lines for the examined T-stubs with two bolts in a row were generally underestimated by Equation (12), with a mean test-to-prediction ratio of 1.12 and a COV of 0.24. On the contrary, the plastic resistances associated with yielding of the bolts were accurately predicted by Equation (13), with a slight overestimation of only 2% on average and a COV of 0.15.

Only a limited number of specimens failed in Mode 1, the majority of which were the T-stubs with sharp corners, due to the larger values of m , as discussed in Section 5. Generally, the specimen capacities were found to be underestimated by Equation (12) when the failure mode was correctly predicted, but overestimated when the failure mode was wrongly predicted. The variability in the prediction accuracy is believed to relate primarily to the value of the distance m , which is the distance between the two plastic hinges (i.e. at the web-to-flange conjunction and the bolt line). Eurocode 3 assumes that the plastic hinge at the bolt line always lies across the centre of the bolt hole, while, in reality, its location is also dependent on the strength of the bolt. In addition, the plastic hinge at the web-to-flange conjunction is assumed to be located at a distance of $0.8a$ from the web, as illustrated in Figure 4, while this location can vary depending on the specimen geometry. Note also that equations for T-stubs with sharp corners are not explicitly included in Eurocode 3.

For Mode 2, Equation (13) generally overestimated the capacities of the T-stubs that were printed continuously, with a mean test-to-prediction ratio of 0.84 and 0.96 and COVs of 0.15 and 0.09 for the T-stubs with rounded and sharp corners respectively. Conversely, Equation (13) yielded conservative predictions for the T-stubs that were printed in two steps (individually), underestimating the capacity of the specimens with rounded and sharp corners by 6% and 5% on average, respectively, with COVs of 0.13 and 0.09, respectively.

7.2. T-stubs with four bolts in a row

Comparisons between the capacity predictions given by Equations (12) and (17) for the yield loads at the bolt line and the bolt, respectively, are presented in Table 9. It can be seen that the failure modes were generally accurately predicted. As also observed for the T-stubs with two bolts, Equation (12) provided conservative capacity predictions, except when the failure modes were not correctly predicted. Meanwhile, Equation (17), which has been specifically devised for T-stubs with four bolts in a row, yielded accurate predictions with only very few exceptions.

7.3. Yielding at the web-to-flange conjunction

The test-to-predicted capacity ratios presented in Tables 8 and 9 show that Equation (16) significantly underestimated the yield load at the web-to-flange junction, by 50% and 42% on average for the T-stubs with two bolts and four bolts in a row, respectively. This

underestimation is attributed to the fact that Equation (16) simplifies the force applied to the flange by the bolt head as a point load applied at the centre of the bolt hole.

An improved model, replicating the force from the bolt head as a point load applied at the bolt head edge (closer to the T-stub web) as shown in Figure 20, is thus proposed for the determination of the load $F_{Rd,prop}$ corresponding to yielding at the conjunction:

$$F_{Rd,prop} = \frac{2M_{pl}}{m - d_w/2} \quad (18)$$

The test-to-prediction ratios yielded by Equation (18) are presented in Tables 8 and 9. It can be observed that, despite the slightly larger scatter, Equation (18) yields considerably more accurate results than Equation (16), with a mean ratio of 0.93 for the T-stubs with two bolts in a row, and with a mean ratio of 0.99 for the T-stubs with four bolts in a row.

8. Conclusions

Eighty tests on WAAM T-stub connections of different printing strategies, bolt configurations and dimensions have been carried out. The development of plastic hinges at critical locations on the T-stub flanges was thoroughly analysed, and a method for the identification of their occurrence has been established. It was found that the first plastic hinge always forms at web-to-flange junction, followed by yielding of either the bolt line or the bolt, with the first to occur determining the failure mode and collapse load of the connection.

Initial gaps between the T-stub flanges, occurring due to the WAAM surface undulations and bowing of the flanges, were found to lead to a reduction in stiffness and premature yielding at the web-to-flange conjunctions due to the absence of prying forces. Following yielding at the web-to-flange conjunction, contact between the flanges was established, leading to a recovery in stiffness until yielding at the second location took place.

It was found that the printing strategy can have a significant influence on the load-carrying capacity of WAAM T-stub connections. The T-stubs with rounded corners were generally stronger than those with sharp corners, while the specimens printed in two steps, rather than continuously, exhibited the highest plastic resistances due to their higher cooling rate.

Finally, the test results were used to evaluate the applicability of current design equations for conventionally manufactured T-stub connections. For the T-stubs with two bolts in a row, the plastic resistance of Mode 1 was found to be underestimated by Eurocode 3, while rather accurate predictions were yielded for Mode 2. Similarly, for the T-stubs with four bolts in a row, conservative capacity predictions were obtained for Mode 1 when the equations of Eurocode 3 were used, while an equation proposed in the literature, specifically devised for T-stubs with 4 bolts, provided slightly unconservative results. The yield load at the web-to-flange conjunction calculated using the Eurocode 3 equation not accounting for prying

actions was found to lead to overly conservative predictions. Thus, a new equation has been proposed, accounting for the bolt head size, resulting in more accurate capacity predictions.

Overall, this research illustrates the feasibility of producing structural steel connections using WAAM and demonstrates that sound structural performance can be achieved. This paves the way for the establishment of more optimised connections that can fully exploit the geometric freedom afforded by WAAM.

Acknowledgements

This research was possible thanks to funding and support from the European Union's Horizon 2020 research and innovation programme under grant agreement No. 820776 'Intelligent data-driven pipeline for the manufacturing of certified metal parts through Direct Energy Deposition process INTEGRADDE'.

References

- [1] L. Gardner, Metal additive manufacturing in structural engineering – review, advances, opportunities and outlook, *Struct.* 47 (2023) 2178–2193.
- [2] I.H. Shah, N. Hadjipantelis, L. Walter, R.J. Myers, L. Gardner, Environmental life cycle assessment of wire arc additively manufactured structural components, *J. Clean. Prod.* 389 (2023) 136071.
- [3] A. Kanyilmaz, A.G. Demir, M. Chierici, F. Berto, L. Gardner, S.Y. Kandukuri, P. Kassabian, T. Kinoshita, A. Laurenti, I. Paoletti, A. du Plessis, S.M.J. Razavi, Role of metal 3D printing to increase quality and resource-efficiency in the construction sector, *Addit. Manuf.* 50 (2022) 102541.
- [4] V. Laghi, M. Palermo, G. Gasparini, T. Trombetti, Computational design and manufacturing of a half-scaled 3D-printed stainless steel diagrid column, *Addit. Manuf.* 36 (2020) 101505.
- [5] V. Laghi, M. Palermo, G. Gasparini, V.A. Girelli, T. Trombetti, Experimental results for structural design of wire-and-arc additive manufactured stainless steel members, *J. Constr. Steel Res.* 167 (2020) 105858.
- [6] L. Gardner, P. Kyvelou, G. Herbert, C. Buchanan, Testing and initial verification of the world's first metal 3D printed bridge, *J. Construct. Steel Res.* 172 (2020) 106233.

- [7] P. Kyvelou, H. Slack, D.D. Mountanou, M.A. Wadee, T.B. Britton, C. Buchanan, L. Gardner, Mechanical and microstructural testing of wire and arc additively manufactured sheet material, *Mater. Des.* 192 (2020) 108675.
- [8] T. Feucht, B. Waldschmitt B, J. Lange, M. Erven, Additive manufacturing of a bridge in situ, *Steel Constr.* 15 (2) (2022) 100–10.
- [9] S.I. Evans, J. Wang, J. Qin, Y. He, P. Shepherd, J. Ding. A review of WAAM for steel construction – Manufacturing, material and geometric properties, design, and future directions, *Struct.* 44 (2022) 1506–1522.
- [10] D. Delgado Camacho, P. Clayton, W.J. O’Brien, C. Seepersad, M. Juenger, R. Ferron, S. Salamone, Applications of additive manufacturing in the construction industry – A forward-looking review, *Autom. Constr.* 89 (2018) 110–119.
- [11] C. Huang, P. Kyvelou, L. Gardner, Stress-strain curves for wire arc additively manufactured steels, *Eng. Struct.* 279 (2023) 115628.
- [12] C. Huang, P. Kyvelou, R Zhang, T.B. Britton, L. Gardner, Mechanical testing and microstructural analysis of wire arc additively manufactured steels, *Mater. Des.* 216 (2022) 110544.
- [13] X. Guo, P. Kyvelou, J. Ye, L.H. Teh, L. Gardner, Experimental investigation of wire arc additively manufactured steel single-lap shear bolted connections, *Thin-Walled Struct.* 181 (2022) 110029.

- [14] X. Guo, P. Kyvelou, J. Ye, L.H. Teh, L. Gardner, Experimental study of double-shear bolted connections between wire arc additively manufactured steel plates, *Eng. Struct.* 281 (2023) 115736.
- [15] J. Lange, T. Feucht, M. Erven. 3D printing with steel – additive manufacturing for connections and structures, *Steel Constr.* 13 (3) (2020) 144–153.
- [16] V. Laghi, M. Palermo, G. Gasparini, V.A. Girelli, T. Trombetti, On the influence of the geometrical irregularities in the mechanical response of wire-and-arc additively manufactured planar elements, *J. Constr. Steel Res.* 178 (2021) 106490.
- [17] J. Ye, P. Kyvelou, F. Gilardi, H. Lu, M. Gilbert, L. Gardner, An End-to-End Framework for the Additive Manufacture of Optimized Tubular Structures, *IEEE Access* 9 (2021) 165476-165489.
- [18] A.C. Faralli, Large deformation of T-stub connection in bolted steel joints, PhD thesis, University College London (2019).
- [19] P. Zoetemeijer, A design method for the tension side of statically-loaded, bolted beam-to-column connections, *Heron*, 20 (1) (1974) 1-59.
- [20] K. Weynand, J.-P. Jaspart, M. Steenhuis, The stiffness model of revised Annex J of Eurocode 3, In: 3rd Inter. workshop on connections (1995) 441-452.
- [21] L. Simões da Silva, A.M. Girão Coelho, A ductility model for steel connections, *J. Construct. Steel Res.*, 57 (2001) 45-70.

- [22] L.S. Silva, A. Santiago, P. Vila Real, A component model for the behaviour of steel joints at elevated temperatures, *J. Construct. Steel Res.* 57 (11) (2001) 1169-1195.
- [23] G.J. Berrospi Aquino, A.M. Gómez Amador, J.H. Alencastre Miranda, J.J. Jiménez de Cisneros Fonfría, A Review of the T-Stub Components for the Analysis of Bolted Moment Joints. *Appl. Sci.* 11 (2021) 10731.
- [24] Eurocode 3: Design of steel structures – Part 1-8: Design of joints, prEN 1993-1-8, Brussels, European Committee for Standardisation (2021).
- [25] M.S. Zhao, C.K. Lee, S.P. Chiew, Tensile behavior of high performance structural steel T-stub joints, *J. Construct. Steel Res.* 122 (2016) 316-325.
- [26] H.X. Yuan, S. Hu, X.X. Du, L. Yang, X.Y. Cheng, M. Theofanous, Experimental behaviour of stainless steel bolted T-stub connections under monotonic loading, *J. Construct. Steel Res.* 152 (2019) 213-224.
- [27] O. Yapici, M. Theofanous, S. Dirar, H. Yuan, Behaviour of ferritic stainless steel bolted T-stubs under tension-part 1: Experimental investigations, *ce/papers* 4 (2021) 866-875.
- [28] Z. Wang, Y. Wang, Y. Zhang, L. Gardner, Y. Ouyang, Experimental investigation and design of extruded aluminium alloy T-stubs connected by swage-locking pins, *Eng. Struct.* 200 (2019) 109675.
- [29] P. Zoetemeijer, A design method for the tension side of statically loaded, bolted beam-to-column connections, *Heron*, 20 (1974) 1-59.

- [30] V. Piluso, C. Faella, G. Rizzano, Ultimate behavior of bolted T-stubs. I: Theoretical model, *J. Struct. Eng.* 127 (6) (2001) 686-693.
- [31] V. Piluso, C. Faella, G. Rizzano, Ultimate behavior of bolted T-stubs. II: Model validation, *J. Struct. Eng.* 127 (6) (2001) 694-704.
- [32] X. Zhao, S. He, S. Yan, Full-range behaviour of T-stubs with various yield line patterns, *J. Construct. Steel Res.* 186 (2021) 106919.
- [33] R. Tartaglia, M. D'Aniello, M. Zimbru, Experimental and numerical study on the T-Stub behaviour with preloaded bolts under large deformations, *Struct.* 27 (2020) 2137-2155.
- [34] Y.O. Özkılıç, The capacities of unstiffened T-stubs with thin plates and large bolts, *J. Construct. Steel Res.* 186 (2021) 106908.
- [35] R.T. Douty, W. McGuire, High strength bolted moment connection, *J. Struct. Div.* 91 (2) (1965) 101-128.
- [36] R.S. Nair, P.C. Birkemoe, W.H. Munse, High strength bolts subject to tension and prying, *J. struct. Div.* 100 (2) (1974) 351-372.
- [37] M. Couchaux, M. Hjiiaj, I. Ryan, A. Bureau, Effect of contact on the elastic behaviour of tensile bolted connections, *J. Constr. Steel Res.* 133 (2017) 459-474.
- [38] A.M. Girão Coelho, L. Simões da Silva, F. Bijlaard, Characterization of the Nonlinear Behavior of Single Bolted T-Stub Connections, In: *Proc. of Connections in Steel Struct.* V, Amsterdam, (2004) 53-64.

- [39] T.J.C. Kombate, K. Taşkın, State-of-the-art review on the behaviour of T-stubs and prying action, *J. Constr. Steel Res.* 191 (2022) 107203.
- [40] H. Agerskov, High-strength bolted connections subject to prying, *J. Struct. Div.* 102 (1) (1976) 161-175.
- [41] C. Faella, V. Piluso, G. Rizzano, Experimental analysis of bolted connections: snug versus preloaded bolts, *J. Struct. Eng.* 124 (7) (1998) 765-774.
- [42] J.A. Swanson, R.T. Leon, Stiffness modelling of bolted T-stub connection components, *J. Struct. Eng.* 127 (5) (2001) 498-505.
- [43] A.M. Girão Coelho, F. Bijlaard, N. Gresnigt, L. Simões da Silva, Experimental assessment of the behaviour of bolted T-stub connections made up of welded plates, *J. Construct. Steel Res.* 60 (2) (2004) 269-311.
- [44] H.X. Yuan, J.D. Gao, M. Theofanous, L. Yang, B.W. Schafer, Initial stiffness and plastic resistance of bolted stainless steel T-stubs in tension, *J. Construct. Steel Res.* 173 (2020) 106239.
- [45] M. Liu, X. Zhu, P. Wang, W. Tuoya, S. Hu, Tension strength and design method for thread-fixed one-side bolted T-stub, *Eng. Struct.* 150 (2017) 918-933.
- [46] Y. Zhang, M. Liu, Q. Ma, Z. Liu, P. Wang, C. Ma, L. Sun, Yield line patterns of T-stubs connected by thread-fixed one-side bolts under tension, *J. Construct. Steel Res.* 166 (2020) 105932.

- [47] A.C. Faralli, M. Latour, P.J. Tan, G.Rizzano, P. Wrobel, Experimental investigation and modelling of T-stubs undergoing large displacements, *J. Construct. Steel Res.* 180 (2021) 106580.
- [48] W. Bao, J. Jiang, Z. Yu, X. Zhou, Mechanical behavior of high-strength bolts in T-stubs based on moment distribution, *Eng. Struct.* 196 (2019) 109334.
- [49] J. Demonceau, K. Weynand, J. Jaspart, C. Müller, Application of Eurocode 3 to steel connections with four bolts per horizontal row, In: *SDSS (Rio de Janeiro)* (2010) 199-206.
- [50] M. Latour, G. Rizzano, A. Santiago, L. Simões da Silva, Experimental analysis and mechanical modelling of T-stubs with four bolts per row, *J. Construct. Steel Res.* 101 (2014) 158-174.
- [51] MX3D, About – MX3D, [online] Available from <https://mx3d.com>, accessed Mar. 15, 2021.
- [52] EN ISO 14341: 2020 Welding consumables – Wire electrodes and weld deposits for gas shielded metal arc welding of non alloy and fine grain steels- Classification, International Organization for Standardization.
- [53] FARO Design ScanArm 2.0 ®, 2018.
- [54] 3D Systems, Geomagic Wrap 2017 (Version 2017.0.2:64) [Software] 2017 3D Systems, Incorporated and its licensors, 2017.
- [55] Rhino 3D, Rhino 3D computer-aided design software (Version 5 SR14 64-bit)

[Software] Robert McNeel & Associates, 2017.

[56] EN ISO 6892-1: 2019 Metallic materials – tensile testing, Part1: Method of test at room temperature, International Organization for Standardization.

[57] LaVision, DaVis (Version 8.4.0) [Software] La Vision GmbH, 2017.

[58] Dassault Systèmes Corp., Abaqus 2019, 2019.

Table 1. Chemical composition (% by weight) of feedstock wire [13]

C	Si	Mn	P	S	Cr	Ni	Mo	Cu	V	Ai	Zr+Ti
0.07	0.85	1.43	0.007	0.006	0.04	0.01	0.01	0.01	0.01	0.01	0.02

Table 2. Mechanical properties (as welded) of feedstock wire [13]

Yield strength (MPa)	Ultimate tensile strength (MPa)	Elongation A5 (%)	Impact energy at -40 °C (J)
471	580	25	73

Table 3. Printing parameters for WAAM T-stubs

Printing parameter	Value
Wire diameter (mm)	1.2
Travel speed (mm/s)	8
Wire feed speed (m/min)	4
Welding voltage (V)	24.8
Welding current (A)	130
Gas flow rate (L/min)	16
Shielding gas	80% Ar + 20% CO ₂
Welding mode	Pulsed
Dwell time (s)	30

Table 4. Measured geometric properties of T-stubs with two bolts in a row

Specimen	Bolt grade	t (mm)	b (mm)	m (mm)	e (mm)	a (mm)
T1-40-0.67-C-R	8.8	8.3	40.7	21.1	20.8	9.3
T1-40-0.67-I-R	8.8	9.3	41.1	24.5	20.4	5.9
T1-40-0.67-C-S	8.8	8.0	41.0	29.8	20.3	-
T1-40-0.67-I-S	8.8	9.1	39.5	29.2	20.9	-
T1-40-2.00-C-R	8.8	8.6	41.7	11.1	40.3	9.6
T1-40-2.00-I-R	8.8	9.1	41.0	14.5	40.9	6.1
T1-40-2.00-C-S	8.8	8.0	40.2	19.9	40.2	-
T1-40-2.00-I-S	8.8	8.7	41.8	19.4	40.8	-
T1-60-0.40-C-R	8.8	8.4	60.5	41.2	20.8	9.8
T1-60-0.40-I-R	8.8	8.8	60.0	44.5	20.8	5.8
T1-60-0.40-C-S	8.8	8.0	59.5	50.0	20.1	-
T1-60-0.40-I-S	8.8	8.9	59.1	49.3	20.4	-
T1-60-0.67-C-R	8.8	8.4	60.5	21.3	20.7	9.4
T1-60-0.67-I-R	8.8	8.8	59.7	24.6	21.1	5.8

T1-60-0.67-C-S	8.8	8.1	60.9	29.9	20.0	-
T1-60-0.67-I-S	8.8	8.9	61.1	29.3	20.5	-
T1-70-0.50-C-R	8.8	8.6	69.2	31.2	20.9	9.7
T1-70-0.50-I-R	8.8	8.8	69.8	34.4	20.3	6.1
T1-70-0.50-C-S	8.8	8.2	70.1	39.8	20.5	-
T1-70-0.50-I-S	8.8	8.9	69.8	39.3	21.1	-
T1-70-0.67-C-R	8.8	8.5	69.6	21.4	20.5	9.5
T1-70-0.67-I-R	8.8	8.9	69.0	25.3	21.1	5.4
T1-70-0.67-C-S	8.8	8.1	70.0	29.8	20.4	-
T1-70-0.67-I-S	8.8	9.0	73.0	29.4	20.9	-
T1-90-0.33-C-R	8.8	7.9	95.7	18.9	11.4	12.1
T1-90-0.33-I-R	8.8	8.9	92.1	24.1	11.0	6.0
T1-90-0.33-C-S	8.8	8.1	91.1	28.6	11.4	-
T1-90-0.33-I-S	8.8	8.8	93.4	28.7	11.3	-
T1-90-0.67-C-R	8.8	8.6	93.9	21.6	23.5	8.7
T1-90-0.67-I-R	8.8	8.8	92.4	26.0	22.3	3.9
T1-90-0.67-C-S	8.8	8.6	102.5	29.3	22.1	-
T1-90-0.67-I-S	8.8	9.0	104.3	29.0	22.4	-
T1-120-0.67-C-R	8.8	7.8	123.6	20.5	19.0	9.8
T1-120-0.67-I-R	8.8	8.9	122.2	27.5	21.0	3.7
T1-120-0.67-C-S	8.8	8.1	119.4	30.4	19.4	-
T1-120-0.67-I-S	8.8	8.8	117.4	30.1	19.9	-
T1-120-1.33-C-R	8.8	7.6	123.0	22.7	39.1	9.4
T1-120-1.33-I-R	8.8	8.5	120.2	24.6	41.1	6.5
T1-120-1.33-C-S	8.8	7.9	121.1	30.9	39.3	-
T1-120-1.33-I-S	8.8	8.9	117.2	30.3	38.8	-
T1-150-0.67-C-R	10.9	7.9	148.1	22.6	18.1	9.8
T1-150-0.67-I-R	10.9	8.8	148.6	25.3	19.8	6.4
T1-150-0.67-C-S	10.9	7.9	153.4	30.8	19.3	-
T1-150-0.67-I-S	10.9	9.0	148.3	30.0	19.9	-
T1-160-0.67-C-R	10.9	8.0	160.5	21.7	19.2	10.7
T1-160-0.67-I-R	10.9	8.6	159.9	25.3	19.3	6.4
T1-160-0.67-C-S	10.9	8.0	158.1	30.8	19.1	-
T1-160-0.67-I-S	10.9	8.9	159.8	30.1	19.9	-
T1-160-1.50-C-R	10.9	8.7	160.1	32.6	59.4	9.3
T1-160-1.50-I-R	10.9	8.8	161.3	35.7	59.3	6.0
T1-160-1.50-C-S	10.9	8.5	161.6	41.1	58.8	-
T1-160-1.50-I-S	10.9	8.7	163.0	40.4	59.2	-

Table 5. Measured geometric properties of T-stubs with four bolts in a row

Specimen	Bolt grade	t (mm)	b (mm)	m (mm)	e_1 (mm)	e_2 (mm)	a (mm)
T2-70-1.13-C-R	8.8	8.6	70.8	30.4	35.0	10.4	9.8
T2-70-1.13-I-R	8.8	8.9	72.3	34.1	34.9	10.6	6.4
T2-70-1.13-C-S	8.8	8.0	69.3	39.6	35.1	10.5	-
T2-70-1.13-I-S	8.8	8.8	71.9	39.2	35.0	10.3	-
T2-70-1.83-C-R	8.8	8.6	69.3	20.2	30.0	25.7	9.3
T2-70-1.83-I-R	8.8	8.9	70.5	23.9	30.0	26.0	5.6
T2-70-1.83-C-S	8.8	8.0	70.8	29.9	30.0	25.3	-
T2-70-1.83-I-S	8.8	8.8	71.1	29.3	30.0	25.6	-
T2-90-1.83-C-R	8.8	8.7	89.9	22.3	30.0	24.3	9.3
T2-90-1.83-I-R	8.8	9.0	85.6	24.6	30.0	25.8	5.8
T2-90-1.83-C-S	8.8	8.7	90.4	30.4	30.0	24.5	-
T2-90-1.83-I-S	8.8	8.8	95.7	30.4	30.0	24.4	-
T2-120-2.75-C-R	8.8	8.1	119.2	12.7	30.6	24.4	8.3
T2-120-2.75-I-R	8.8	9.0	122.2	14.6	30.3	24.5	6.0
T2-120-2.75-C-S	8.8	8.2	120.3	20.6	29.9	24.5	-
T2-120-2.75-I-S	8.8	8.8	118.2	20.3	30.0	24.6	-
T2-120-1.83-C-R	8.8	8.6	122.1	20.8	30.0	25.4	9.0
T2-120-1.83-I-R	8.8	9.0	121.7	23.6	30.0	25.7	5.9
T2-120-1.83-C-S	8.8	8.0	120.7	29.4	30.0	25.3	-
T2-120-1.83-I-S	8.8	8.9	118.6	29.4	30.0	25.4	-
T2-140-1.83-C-R	10.9	8.0	139.2	19.7	30.0	24.8	10.0
T2-140-1.83-I-R	10.9	8.9	140.4	24.2	30.0	25.0	5.8
T2-140-1.83-C-S	10.9	7.8	140.5	29.4	30.0	24.6	-
T2-140-1.83-I-S	10.9	8.9	142.9	29.2	30.0	24.4	-
T2-140-2.75-C-R	10.9	8.6	142.0	9.6	30.0	25.8	9.0
T2-140-2.75-I-R	10.9	8.8	142.6	13.9	30.0	26.0	5.5
T2-140-2.75-C-S	10.9	8.2	140.7	19.8	30.0	25.6	-
T2-140-2.75-I-S	10.9	8.9	140.9	19.1	30.0	25.8	-

Table 6. Average mechanical properties obtained from as-built WAAM tensile coupons

E (GPa)	f_y (MPa)	f_u (MPa)	ϵ_u	ϵ_f
215	306	416	0.18	0.36

Table 7. Evaluation of M_x relative to the theoretical plastic moment M_{pl} for varying multiples of the yield strain ϵ_y

		M_x/M_{pl}					
ϵ_{yy}	ϵ_y	$2\epsilon_y$	$3\epsilon_y$	$4\epsilon_y$	$5\epsilon_y$	$6\epsilon_y$	$7\epsilon_y$
Mean	0.60	0.85	0.94	0.97	0.98	0.99	0.99
COV	0.020	0.009	0.003	0.002	0.002	0.001	0.001

Table 8. Summary of experimental results for T-stubs with two bolts in a row and comparisons with design equations (FM_{Test} = test failure mode and FM_{theo} = theoretical failure mode in brackets if different from the test results)

Specimen	$F_{y,C}$ (kN)	$F_{y,BL}$ (kN)	$F_{y,B}$ (kN)	$F_{coll,test}$ (kN)	F_u (kN)	FM_{Test}	FM_{Theo}	$\frac{F_{y,C}}{F_{Rd,np}}$	$\frac{F_{y,BL}}{F_{Rd,1}}$	$\frac{F_{y,B}}{F_{Rd,2}}$	$\frac{F_{y,C}}{F_{Rd,prop}}$
								Eq.(16)	Eq.(12)	Eq.(13)	Eq.(18)
T1-40-0.67-C-R	34.21	58.35	41.58	41.58	91.01	2	(1)	1.68	-	0.59	0.89
T1-40-2.00-C-R	61.90	95.09	88.64	88.64	121.67	2	2	1.47	-	1.03	0.16
T1-60-0.40-C-R	28.29	44.82	46.68	44.82	75.30	1	1	1.79	1.23	-	1.36
T1-60-0.67-C-R	52.41	77.29	72.36	72.36	100.95	2	2	1.70	-	0.96	0.91
T1-70-0.50-C-R	40.53	68.51	58.41	58.41	93.06	2	(1)	1.61	-	0.92	1.10
T1-70-0.67-C-R	59.81	98.58	62.47	62.47	103.72	2	2	1.68	-	0.81	0.90
T1-90-0.33-C-R	54.10	60.24	69.08	60.24	105.62	1	(2)	1.29	0.53	-	0.61
T1-90-0.67-C-R	70.33	105.31	71.95	71.95	123.39	2	2	1.42	-	0.83	0.77
T1-120-0.67-C-R	59.52	79.86	70.55	70.55	115.29	2	2	1.27	-	0.84	0.65
T1-120-1.33-C-R	68.07	84.18	68.02	68.02	122.81	2	2	1.29	-	0.77	0.72
T1-150-0.67-C-R	62.62	98.84	75.70	75.70	131.33	2	2	1.24	-	0.74	0.77
T1-160-0.67-C-R	70.41	96.70	92.89	92.89	136.71	2	2	1.46	-	0.95	0.79
T1-160-1.50-C-R	81.22	103.17	105.57	103.17	138.07	1	(2)	1.42	0.80	-	0.99
Mean								1.49	0.85	0.84	0.82
COV								0.13	0.42	0.15	0.34
T1-40-0.67-I-R	34.51	77.65	51.09	51.09	93.36	2	(1)	1.57	-	0.72	0.94
T1-40-2.00-I-R	80.97	101.55	90.05	90.05	128.77	2	2	2.26	-	1.12	0.71
T1-60-0.40-I-R	24.69	58.62	45.68	45.68	73.90	2	(1)	1.53	-	0.96	1.19
T1-60-0.67-I-R	43.49	101.29	63.89	63.89	105.15	2	(1)	1.52	-	1.11	0.91
T1-70-0.50-I-R	38.67	90.44	55.53	55.53	93.10	2	(1)	1.60	-	1.29	1.14
T1-70-0.67-I-R	48.31	103.21	72.44	72.44	106.31	2	2	1.46	-	1.00	0.89
T1-90-0.33-I-R	75.08	97.90	61.14	61.14	98.99	2	2	1.64	-	1.17	0.96

T1-90-0.67-I-R	59.73	98.93	86.37	86.37	122.98	2	2	1.40	-	1.09	0.87
T1-120-0.67-I-R	75.27	116.41	77.96	77.96	120.44	2	2	1.41	-	0.94	0.90
T1-120-1.33-I-R	81.91	131.13	99.60	99.60	135.33	2	2	1.50	-	1.09	0.90
T1-150-0.67-I-R	58.87	120.44	110.80	110.80	153.41	2	2	1.05	-	1.11	0.64
T1-160-0.67-I-R	72.46	115.62	110.78	110.78	149.01	2	2	1.36	-	1.13	0.83
T1-160-1.50-I-R	88.43	108.10	113.63	108.10	135.40	1	(2)	1.67	0.92	-	1.20
Mean								1.54	0.92	1.06	0.93
COV								0.17	-	0.13	0.18
T1-40-0.67-C-S	33.46	41.19	51.03	41.19	82.60	1	1	2.46	1.28	-	1.64
T1-40-2.00-C-S	29.70	63.77	60.50	60.50	103.24	1	1	1.51	1.32	-	0.75
T1-60-0.40-C-S	19.55	35.52	42.26	35.52	69.50	1	1	1.69	1.35	-	1.35
T1-60-0.67-C-S	34.89	48.52	51.30	48.52	90.22	1	1	1.71	1.49	-	1.14
T1-70-0.50-C-S	28.19	57.80	56.29	56.29	79.88	2	(1)	1.57	-	1.01	1.18
T1-70-0.67-C-S	39.54	71.50	45.10	45.10	92.33	2	(1)	1.68	-	1.01	1.12
T1-90-0.33-C-S	42.50	71.82	55.18	55.18	91.95	2	2	1.33	-	0.99	0.87
T1-90-0.67-C-S	52.58	95.45	66.23	66.23	102.32	2	2	1.31	-	0.97	0.87
T1-120-0.67-C-S	57.77	89.17	67.01	67.01	106.21	2	2	1.47	-	1.09	0.99
T1-120-1.33-C-S	55.90	83.60	67.07	67.07	118.44	2	2	1.50	-	0.92	1.02
T1-150-0.67-C-S	53.49	78.65	78.38	78.38	130.63	2	2	1.27	-	0.79	0.86
T1-160-0.67-C-S	51.50	81.85	79.64	79.64	129.71	2	2	1.20	-	0.92	0.81
T1-160-1.50-C-S	52.01	95.42	81.88	81.88	143.58	1	1	1.21	0.91	-	0.92
Mean								1.53	1.27	0.96	1.04
COV								0.22	0.17	0.09	0.24
T1-40-0.67-I-S	26.50	42.62	54.73	42.62	82.08	1	1	1.56	1.06	-	1.03
T1-40-2.00-I-S	33.05	72.35	80.13	72.35	106.90	1	1	1.31	1.17	-	0.64
T1-60-0.40-I-S	22.78	46.28	57.23	46.28	71.72	1	1	1.58	1.41	-	1.26
T1-60-0.67-I-S	38.88	86.67	42.93	42.93	91.40	2	(1)	1.54	-	0.92	1.02
T1-70-0.50-I-S	33.95	63.48	48.03	48.03	87.71	1	1	1.59	1.29	-	1.19

T1-70-0.67-I-S	43.84	95.19	57.49	57.49	98.07	2	2	1.44	-	1.15	0.95
T1-90-0.33-I-S	54.50	83.77	66.23	66.23	95.72	2	2	1.41	-	1.05	0.92
T1-90-0.67-I-S	65.75	111.96	68.76	68.76	111.81	2	2	1.48	-	1.19	0.97
T1-120-0.67-I-S	60.33	84.92	70.46	70.46	109.14	2	2	1.30	-	1.06	0.87
T1-120-1.33-I-S	62.73	108.88	77.19	77.19	110.36	2	2	1.33	-	0.97	0.89
T1-150-0.67-I-S	67.99	105.91	95.03	95.03	136.30	2	2	1.23	-	0.99	0.82
T1-160-0.67-I-S	73.08	104.04	99.37	99.37	141.53	2	2	1.34	-	1.07	0.90
T1-160-1.50-I-S	70.71	100.94	95.29	95.29	143.71	1	1	1.50	0.98	-	1.13
Mean								1.43	1.18	1.05	0.97
COV								0.08	0.15	0.09	0.17
Mean								1.50	1.12	0.98	0.94
COV								0.16	0.24	0.15	0.24

Table 9. Summary of experimental results for T-stubs with four bolts in a row and comparisons with design equations (FM_{Test} = test failure mode and FM_{theo} = theoretical failure mode in brackets if different from the test results)

Specimen	$F_{y,C}$ (kN)	$F_{y,BL}$ (kN)	$F_{y,B}$ (kN)	$F_{coll,test}$ (kN)	F_u (kN)	FM_{Test}	FM_{Theo}	$\frac{F_{y,C}}{F_{Rd,np}}$	$\frac{F_{y,BL}}{F_{Rd,1}}$	$\frac{F_{y,B}}{F_{Rd,2}}$	$\frac{F_{y,C}}{F_{Rd,prop}}$
								Eq.(16)	Eq.(12)	Eq.(17)	Eq.(18)
T2-70-1.13-C-R	43.64	62.22	73.31	62.22	112.99	1	1	1.67	1.05	-	1.17
T2-70-1.83-C-R	53.68	87.21	79.37	79.37	119.73	2	2	1.38	-	0.90	0.97
T2-90-1.83-C-R	60.85	103.49	88.21	88.21	128.28	2	2	1.32	-	0.99	0.92
T2-120-2.75-C-R	90.84	140.40	114.31	114.31	140.96	2	2	1.62	-	1.12	1.14
T2-120-1.83-C-R	88.02	110.86	88.88	88.88	130.68	2	2	1.41	-	0.91	0.99
T2-140-1.83-C-R	86.69	96.44	93.59	93.59	164.59	2	2	1.59	-	0.83	1.11
T2-140-2.75-C-R	116.07	148.65	122.86	122.86	186.83	2	2	1.85	-	0.95	1.29
Mean								1.55	-	0.95	1.08
COV								0.12	-	0.10	0.12

T2-70-1.13-I-R	50.42	80.24	80.33	80.24	109.51	1	1	1.95	1.39	-	1.36
T2-70-1.83-I-R	46.21	101.38	80.83	80.83	124.41	2	2	1.30	-	0.97	0.91
T2-90-1.83-I-R	60.28	103.64	84.87	84.87	129.45	2	2	1.40	-	0.99	0.98
T2-120-2.75-I-R	92.27		110.84	110.84	148.72	2	2	1.35	-	1.06	0.95
T2-120-1.83-I-R	71.16		97.20	97.20	131.95	2	2	1.10	-	1.01	0.77
T2-140-1.83-I-R	60.37	135.87	115.57	115.57	153.11	2	2	0.89	-	1.01	0.63
T2-140-2.75-I-R	69.18	185.16	116.08	116.08	194.96	2	2	1.04	-	0.93	0.73
Mean								1.29	-	1.00	0.90
COV								0.27	-	0.05	0.27
T2-70-1.13-C-S	42.18	51.45	58.00	51.45	107.93	1	1	2.46	1.36	-	1.72
T2-70-1.83-C-S	40.99	65.20	70.31	65.20	119.94	1	1	1.77	1.24	-	1.24
T2-90-1.83-C-S	48.83	81.65	77.61	77.61	117.73	2	2	1.42	-	1.00	0.99
T2-120-2.75-C-S	69.10	102.98	87.48	87.48	139.89	2	2	1.21	-	0.92	0.85
T2-120-1.83-C-S	53.40	81.45	81.81	81.45	124.77	1	(2)	1.33	0.89	-	0.93
T2-140-1.83-C-S	56.14	80.59	86.10	80.59	131.99	1	(2)	1.25	0.79	-	0.87
T2-140-2.75-C-S	69.53	141.28	121.61	121.61	133.14	2	2	1.21	-	1.06	0.84
Mean								1.52	1.07	0.99	1.06
COV								0.30	0.26	0.07	0.30
T2-70-1.13-I-S	31.07	57.37	62.98	57.37	105.19	1	1	1.43	1.20	-	1.00
T2-70-1.83-I-S	37.17	84.95	96.54	84.95	117.39	1	1	1.28	1.29	-	0.90
T2-90-1.83-I-S	52.58	99.06	80.30	80.30	118.13	2	2	1.40	-	1.01	0.98
T2-120-2.75-I-S	79.36	120.27	86.19	86.19	138.81	2	2	1.21	-	0.87	0.85
T2-120-1.83-I-S	54.38	110.22	85.67	85.67	128.49	2	2	1.11	-	1.00	0.77
T2-140-1.83-I-S	75.68	113.08	80.40	80.40	134.97	2	2	1.28	-	0.76	0.89
T2-140-2.75-I-S	94.36	152.42	118.90	118.90	164.91	2	2	1.40	-	1.00	0.98
Mean								1.30	1.24	0.93	0.91
COV								0.09	0.05	0.12	0.09
Mean								1.42	1.15	0.96	0.99
COV								0.22	0.19	0.09	0.22

1 **Table 10.** Comparisons between the yield loads of the four different printing strategies

Printing strategy i		$\frac{F_{y,C,i}}{tb} / \frac{F_{y,C,C-R}}{tb}$	$\frac{F_{y,BL,i}}{tb} / \frac{F_{y,BL,C-R}}{tb}$	$\frac{F_{y,B,i}}{tb} / \frac{F_{y,B,C-R}}{tb}$	$\frac{F_{coll,test,i}}{tb} / \frac{F_{coll,test,C-R}}{tb}$
C-R	Mean	1.00	1.00	1.00	1.00
	COV	-	-	-	-
I-R	Mean	0.93	1.18	1.07	1.09
	COV	0.21	0.13	0.12	0.12
C-S	Mean	0.77	0.87	0.99	0.94
	COV	0.17	0.15	0.16	0.11
I-S	Mean	0.78	0.95	1.01	0.96
	COV	0.15	0.14	0.20	0.14

2 Key: C-R = Continuously printed with rounded corners, I-R = Flanges and web individually
 3 printed with rounded corners, C-S = Continuously printed with sharp corners, I-S= Flanges
 4 and web individually printed with sharp corners

5

6

7

8

9

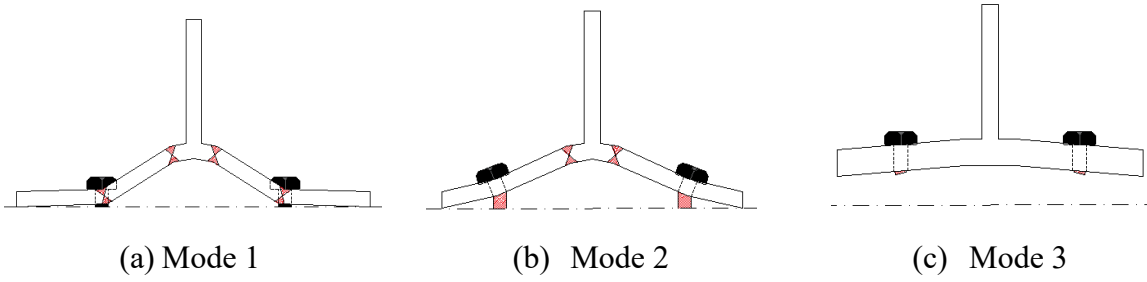
10

11

12

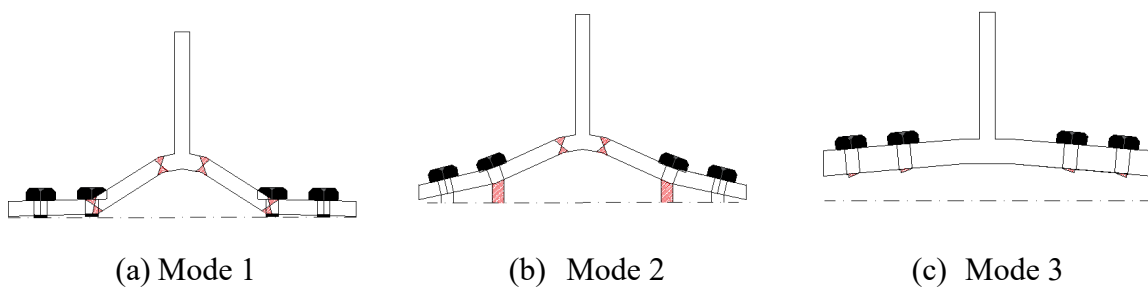
13

14



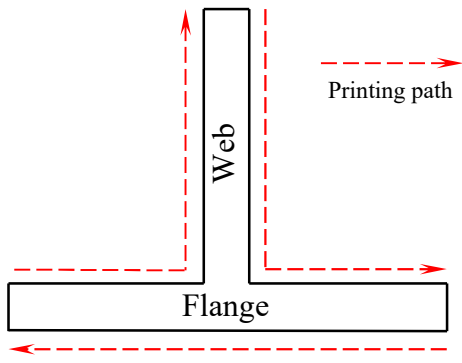
15 **Figure 1.** Plastic failure mechanisms for T-stubs with 2 bolts in a row, as defined in EN
 16 1993-1-8 [24]

17

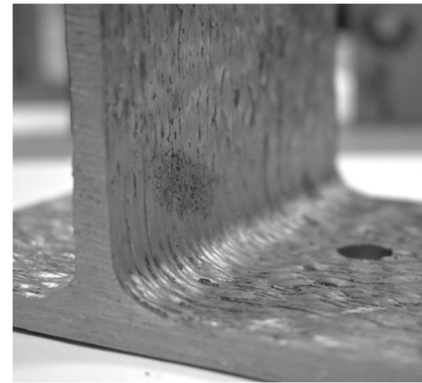
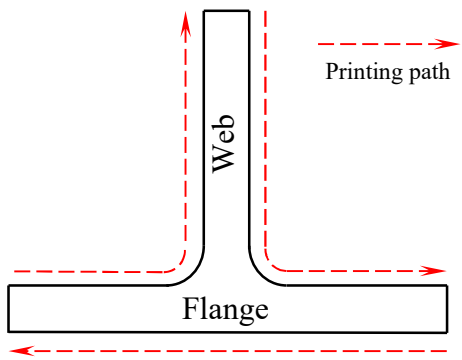


18 **Figure 2.** Plastic failure mechanisms for T-stubs with 4 bolts in a row, as defined in [49]

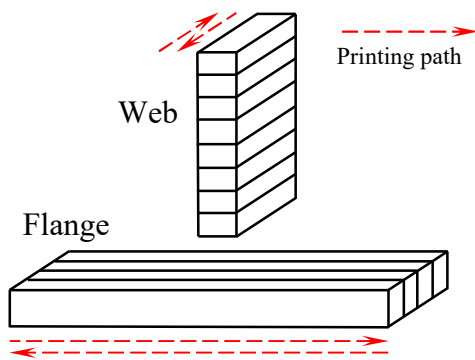
19



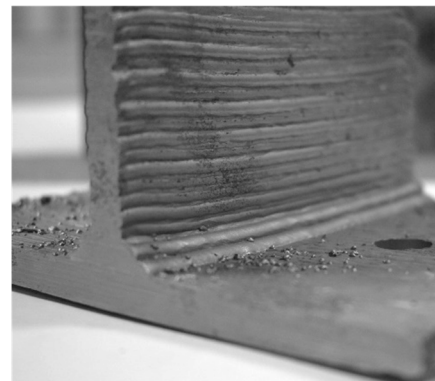
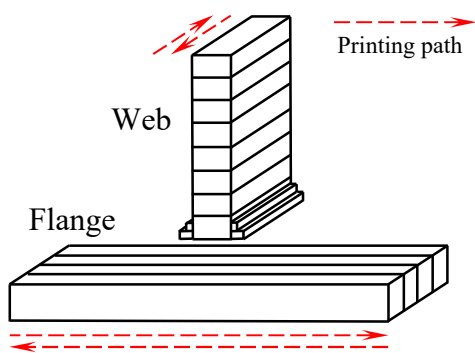
(a) Sharp corners, flanges and web continuously printed



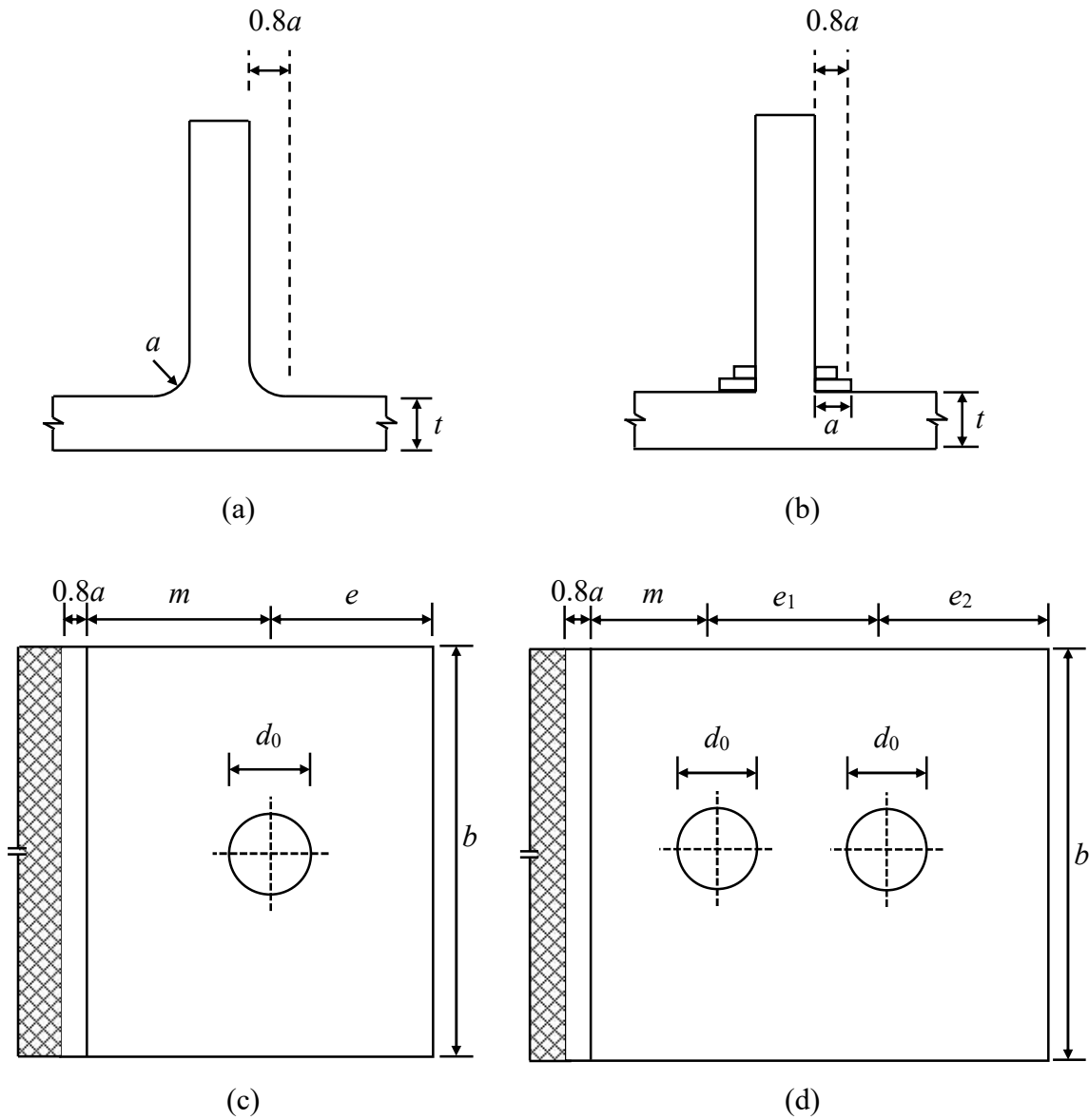
(b) Rounded corners, flanges and web continuously printed



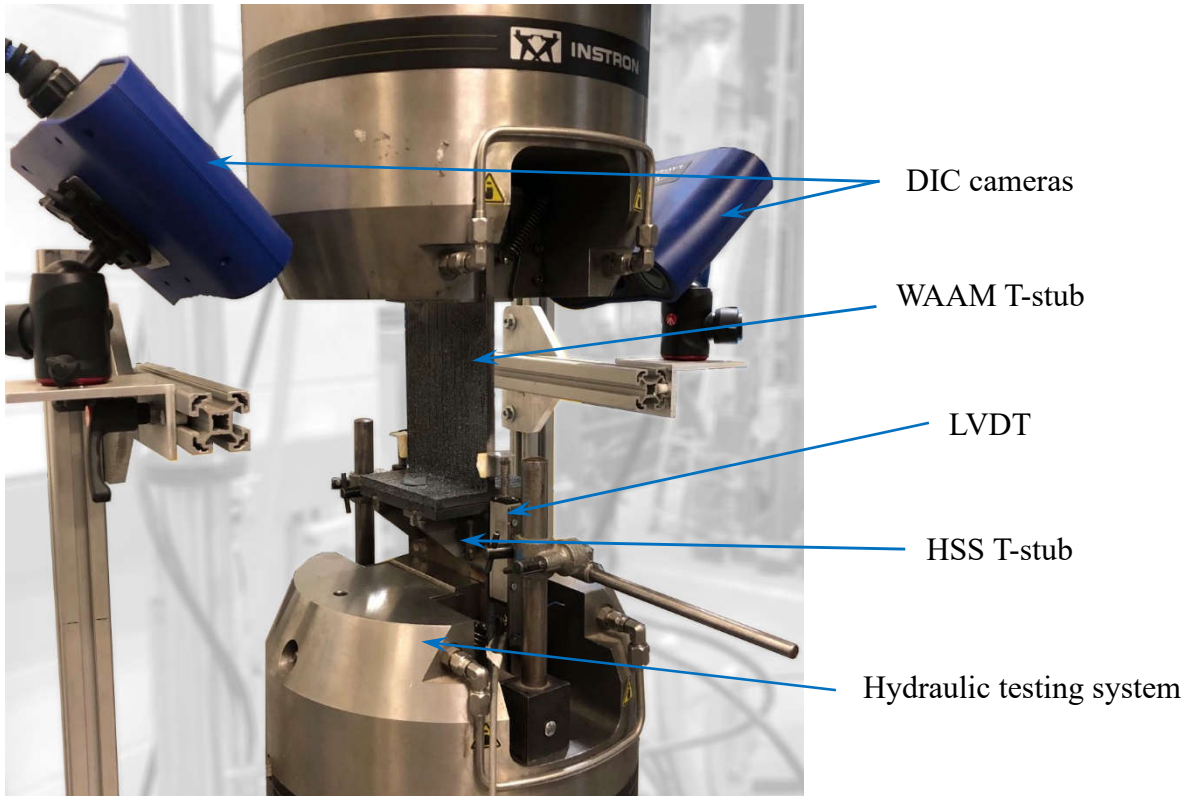
(c) Sharp corners, flanges and web individually printed



(d) Rounded (stepped) corners, flanges and web individually printed

Figure 3. Different printing strategies

21 **Figure 4.** Geometrical configuration of different types of T-stub specimens: (a) continuously
 22 printed with rounded corners, (b) with web and flange individually printed with rounded
 23 (stepped) corners, (c) with two bolts in a row and (d) with four bolts in a row

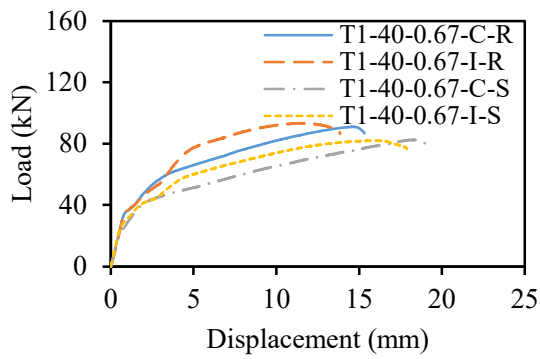


25

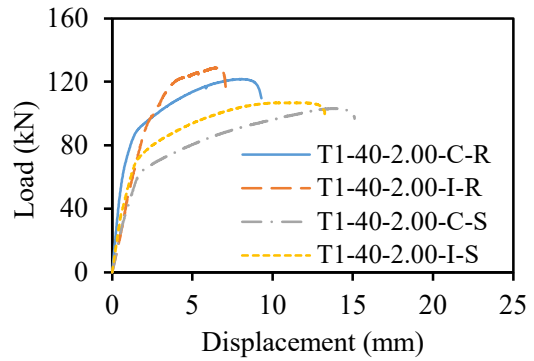
26

Figure 5. T-stub test setup

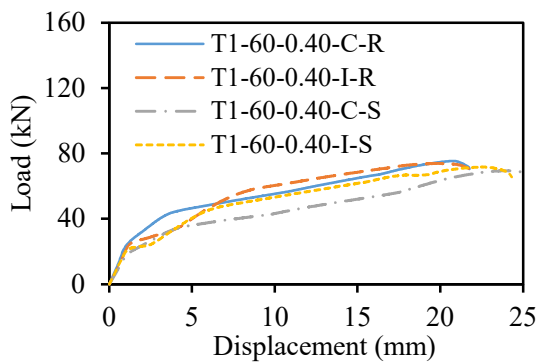
27



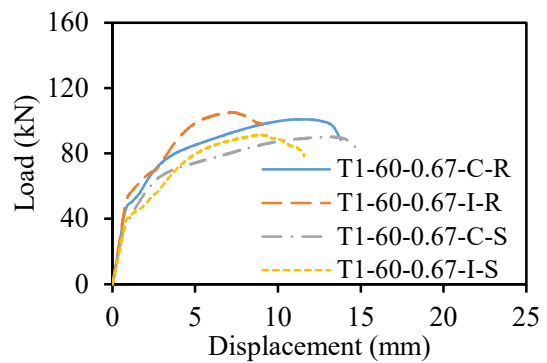
(a) T1-40-0.67



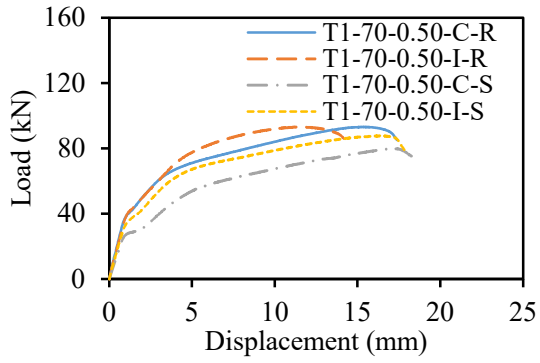
(b) T1-40-2.00



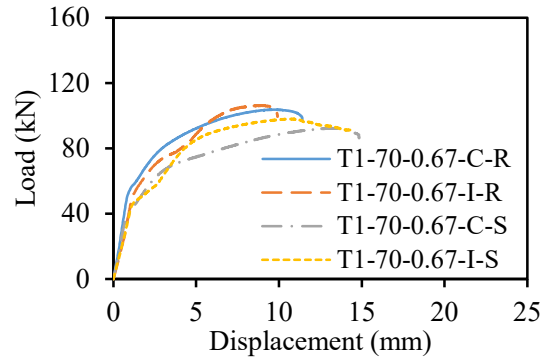
(c) T1-60-0.40



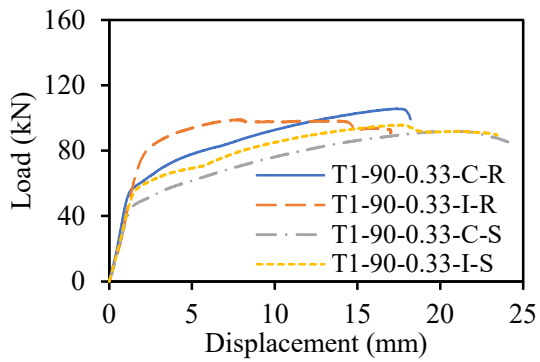
(d) T1-60-0.67



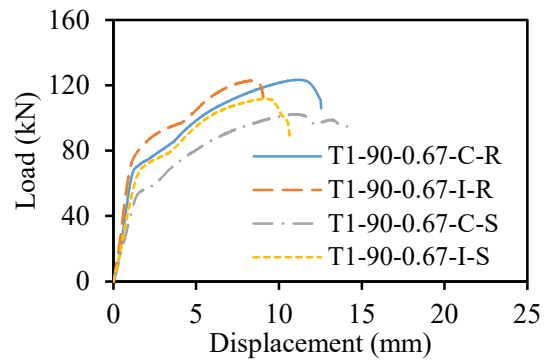
(e) T1-70-0.50



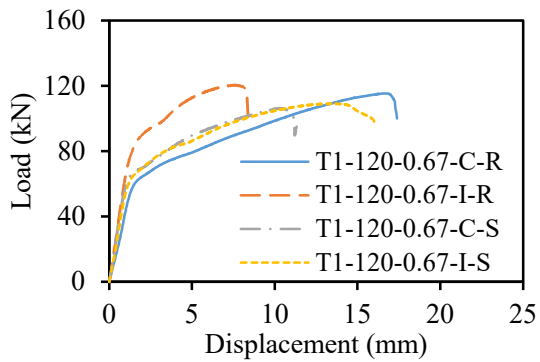
(f) T1-70-0.67



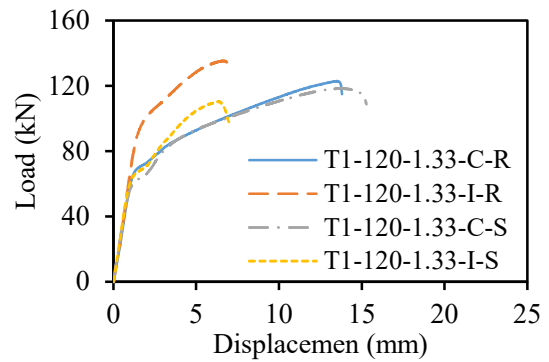
(g) T1-90-0.33



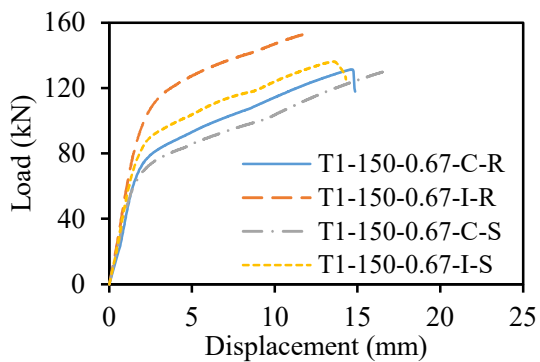
(h) T1-90-0.67



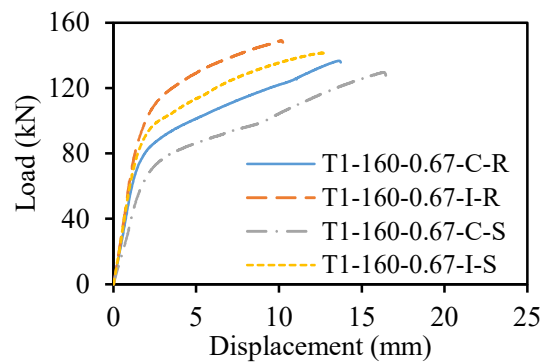
(i) T1-120-0.67



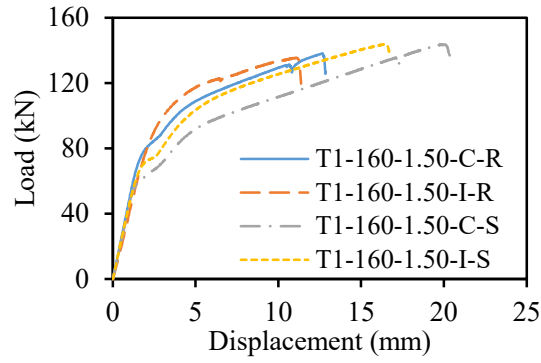
(j) T1-120-1.33



(k) T1-150-0.67



(l) T1-160-0.67



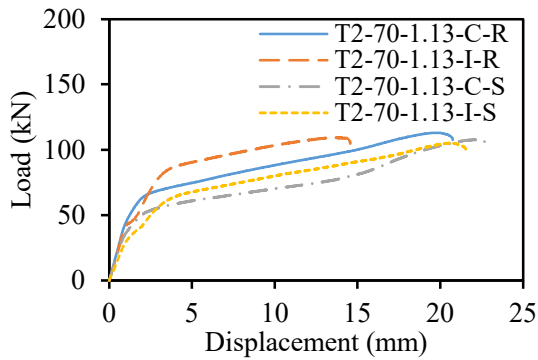
(m)T1-160-1.50

28

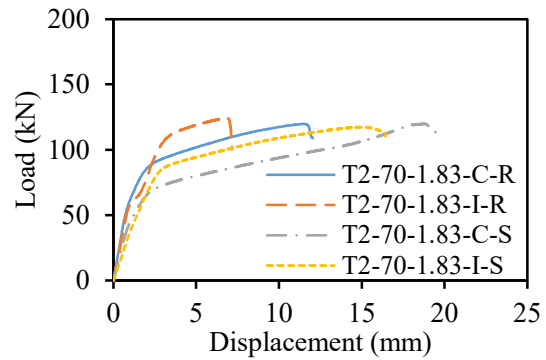
Figure 6. Load-displacement curves of tested T-stubs with two bolts in a row

29

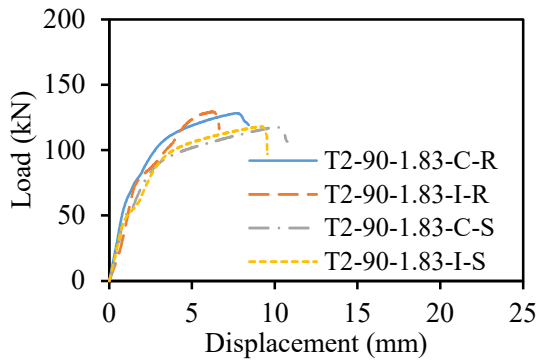
30



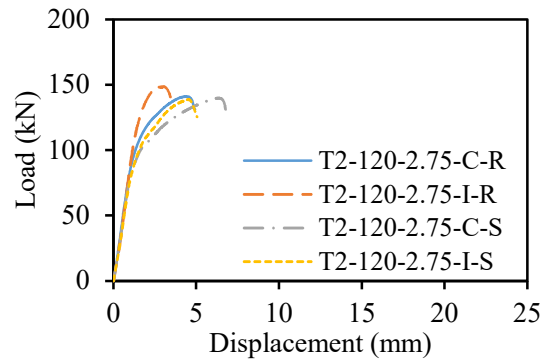
(a) T2-70-1.13



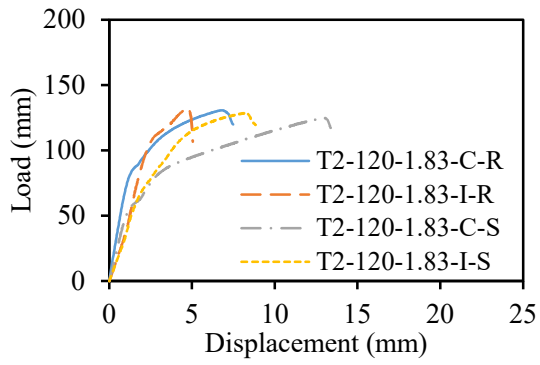
(b) T2-70-1.83



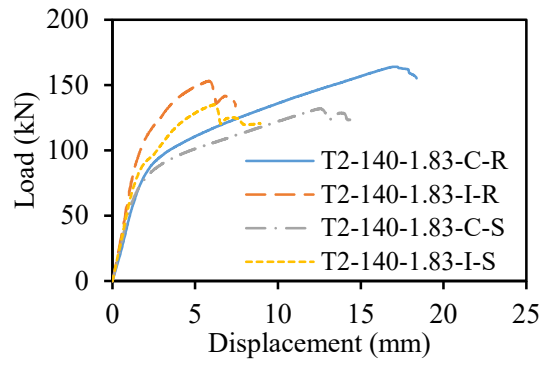
(c) T2-90-1.83



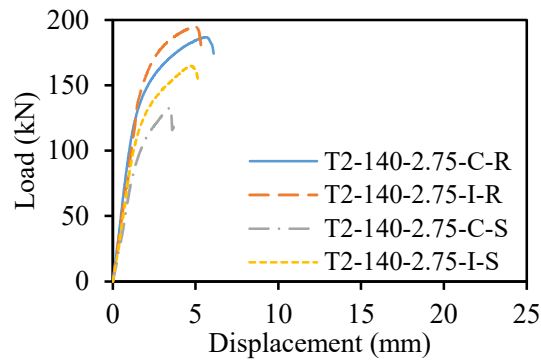
(d) T2-120-2.75



(e) T2-120-1.83



(f) T2-140-1.83



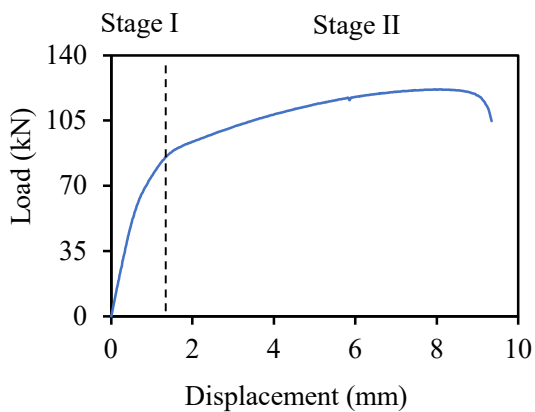
(g) T2-140-2.75

31 **Figure 7.** Load-displacement curves of tested T-stubs with four bolts in a row

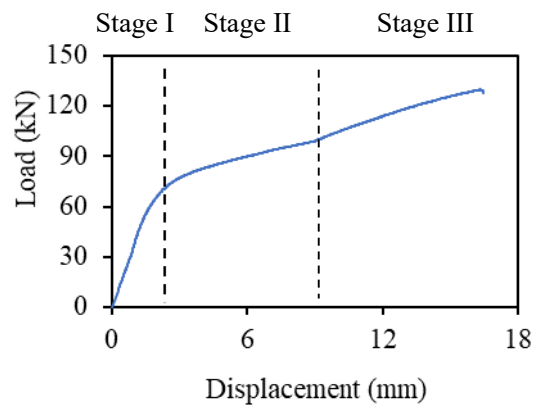
32

33

34



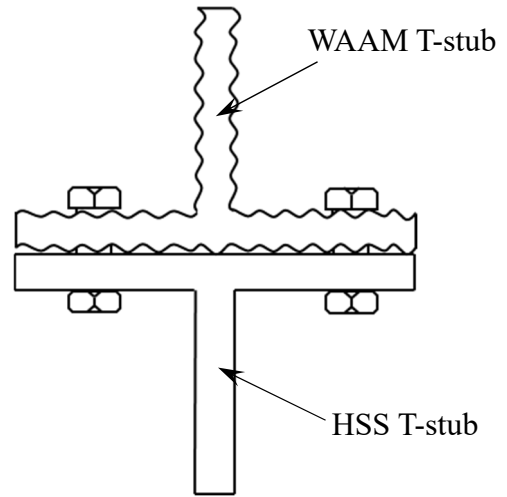
(a) Conventional two-stage behaviour
(Specimen T1-40-2.00-C-R)



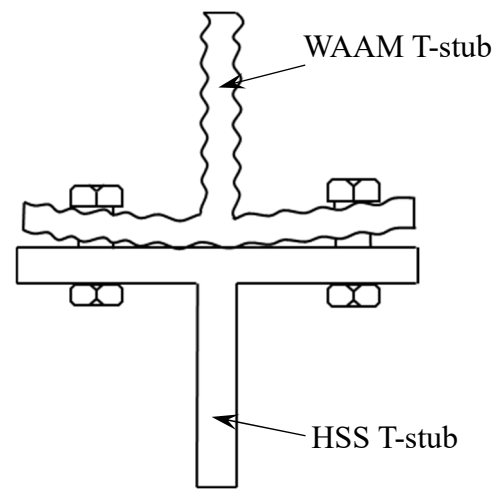
(b) Conventional three-stage behaviour
(Specimen T1-160-0.67-C-S)

35

Figure 8. Typical load-displacement curves



(a) Gap caused by surface undulations

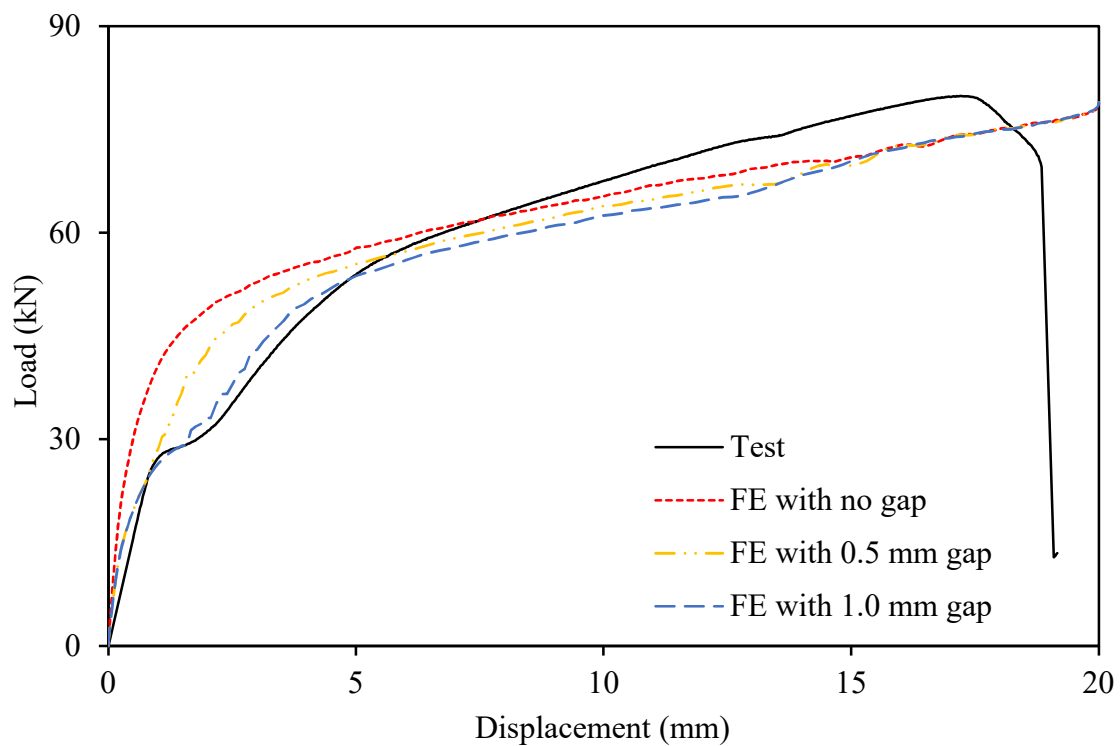


(b) Gap caused by flange bowing

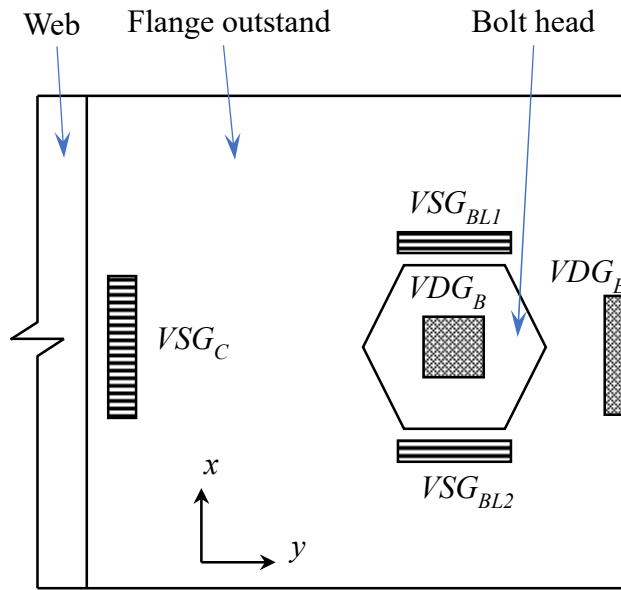
Figure 9. Gaps between the T-stub flanges

36

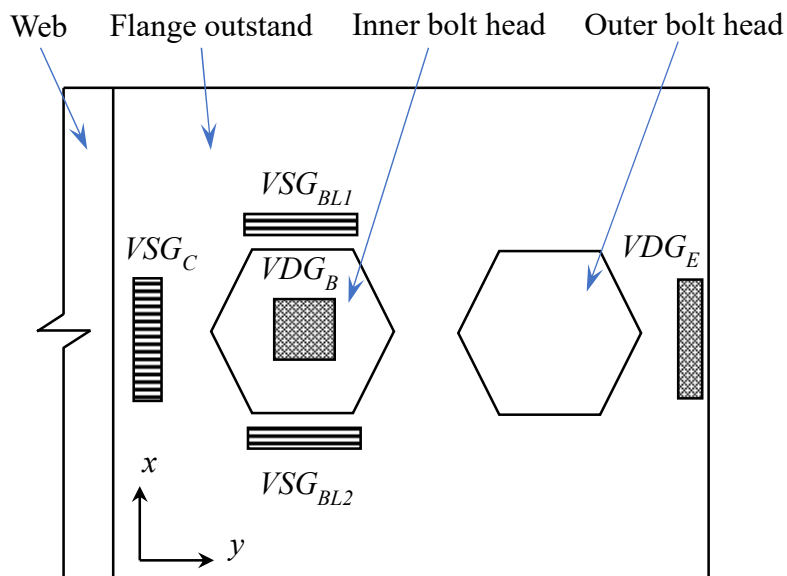
37



38 **Figure 10.** Influence of increasing gap size between T-stub flanges on the load-displacement
 39 curve of a typical specimen, based on preliminary FE simulations (Specimen T1-70-50-C-S)
 40



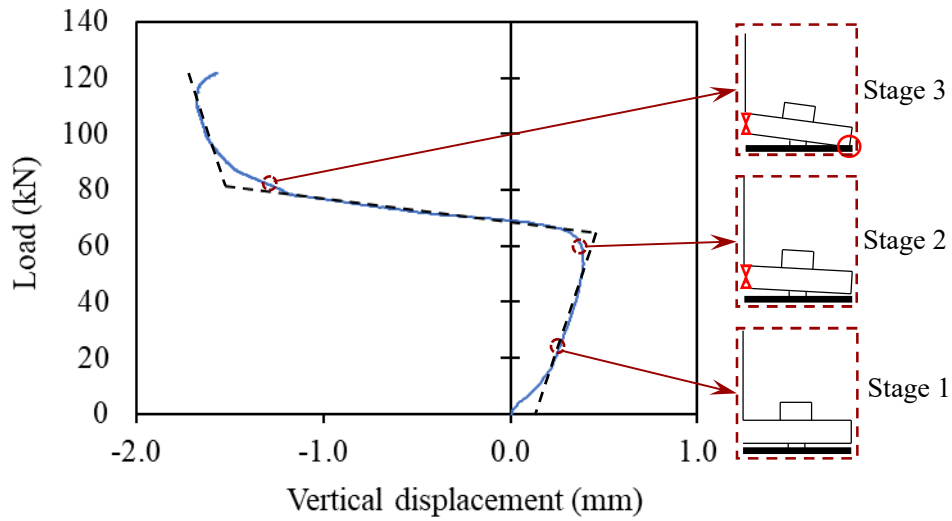
(a) T-stubs with two bolts in a row



(b) T-stubs with four bolts in a row

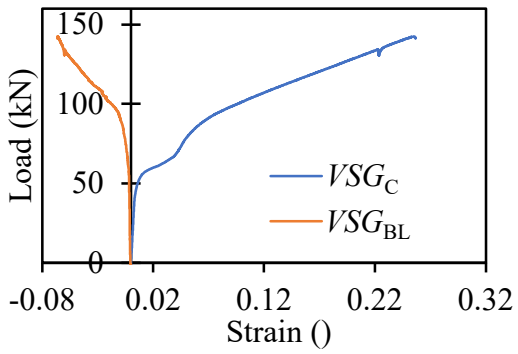
41 **Figure 11.** Location of virtual strain and displacement gauges on flange outstands of T-stubs
 42 with (a) two bolts in a row and (b) four bolts in a row (VSG: virtual strain gauge, VDG:
 43 virtual displacement gauge, C: web-to-flange junction, BL: bolt line, B: bolt and E: flange
 44 end)

45

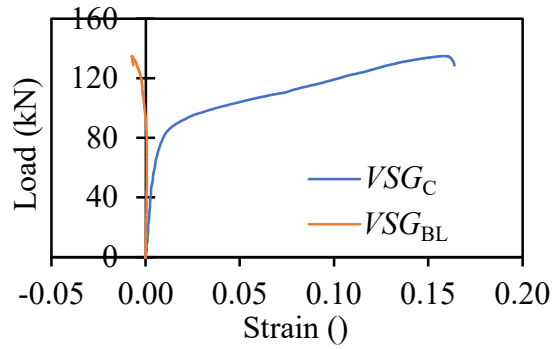


46
47
48
49

Figure 12. Load-vertical displacement of the flange end of Specimen T1-120-1.33-C-R, with illustration of key points



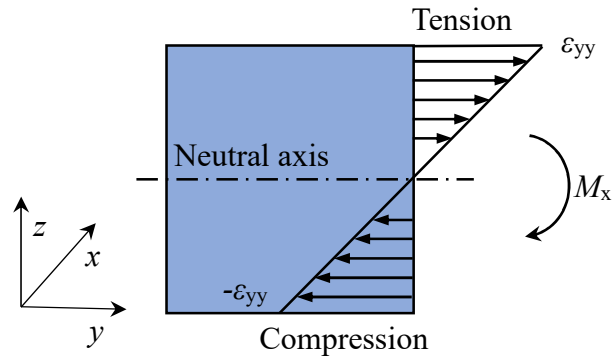
(a) Specimen T1-160-1.50-C-S



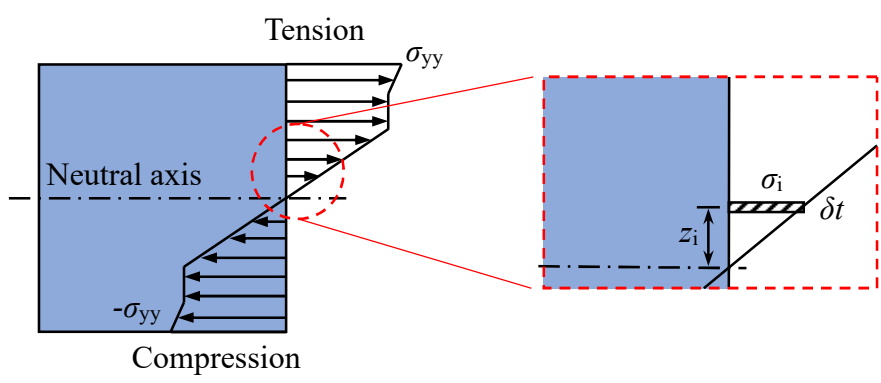
(b) Specimen T1-120-1.33-I-R

50
51

Figure 13. Typical load-strain curves at the web-to-flange conjunction and the bolt line



(a) Strain distribution

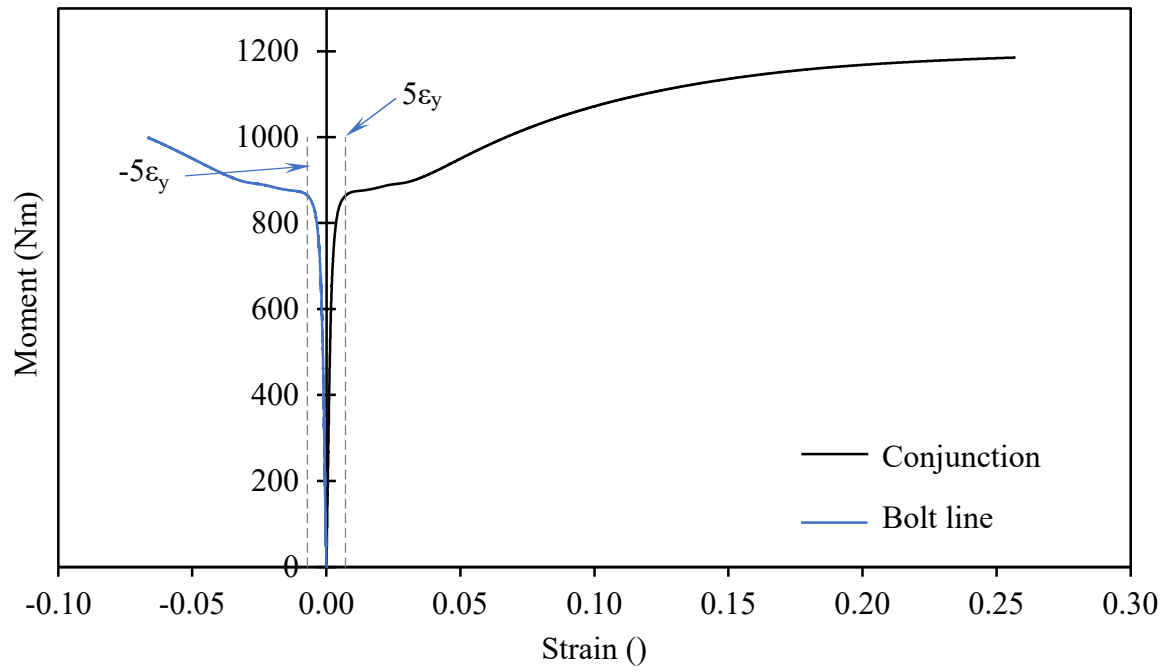


(b) Stress distribution

52

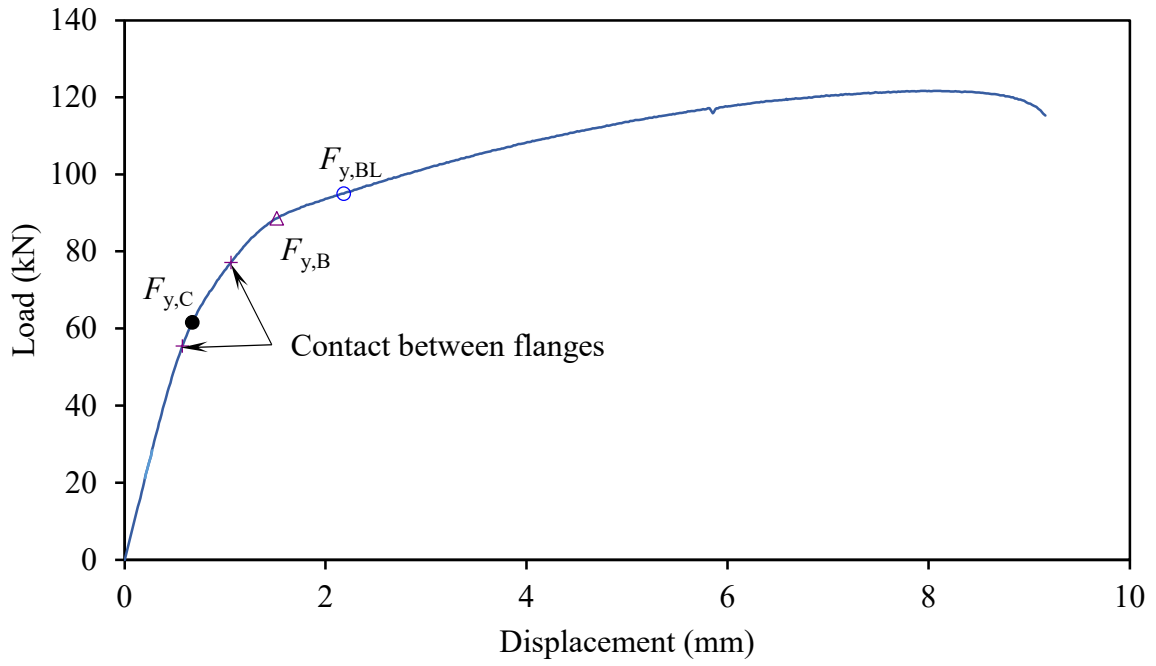
Figure 14. Strain and stress distributions through flange thickness

53

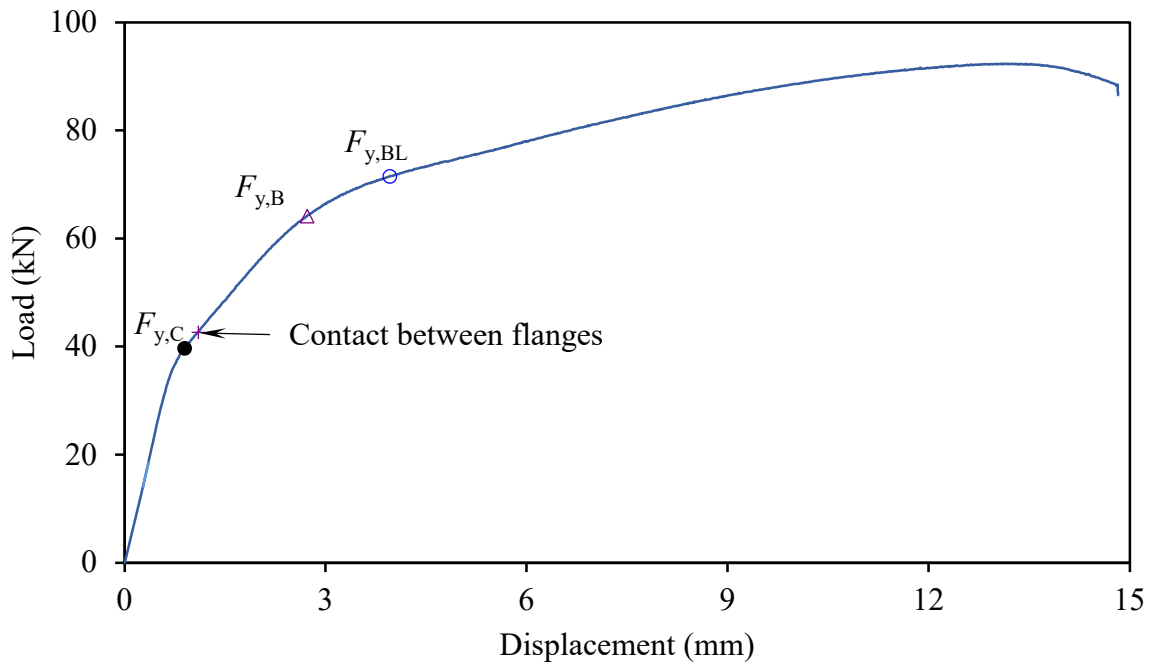


54
55
56

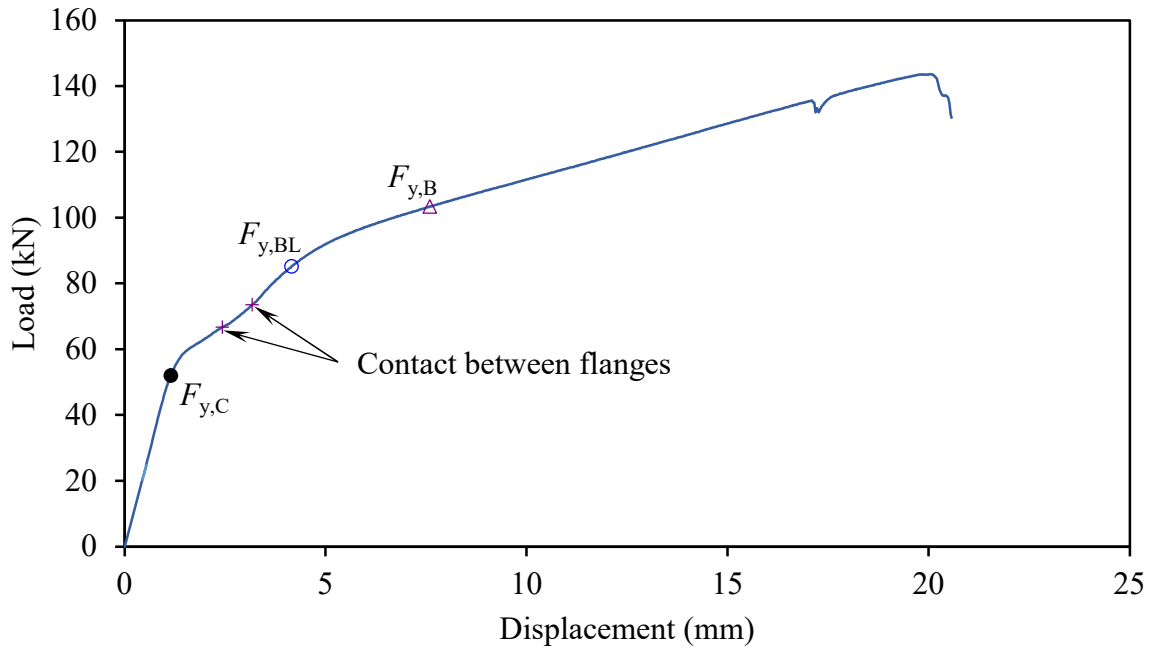
Figure 15. Moment-strain curves at critical locations (Specimen T1-160-1.50-C-S)



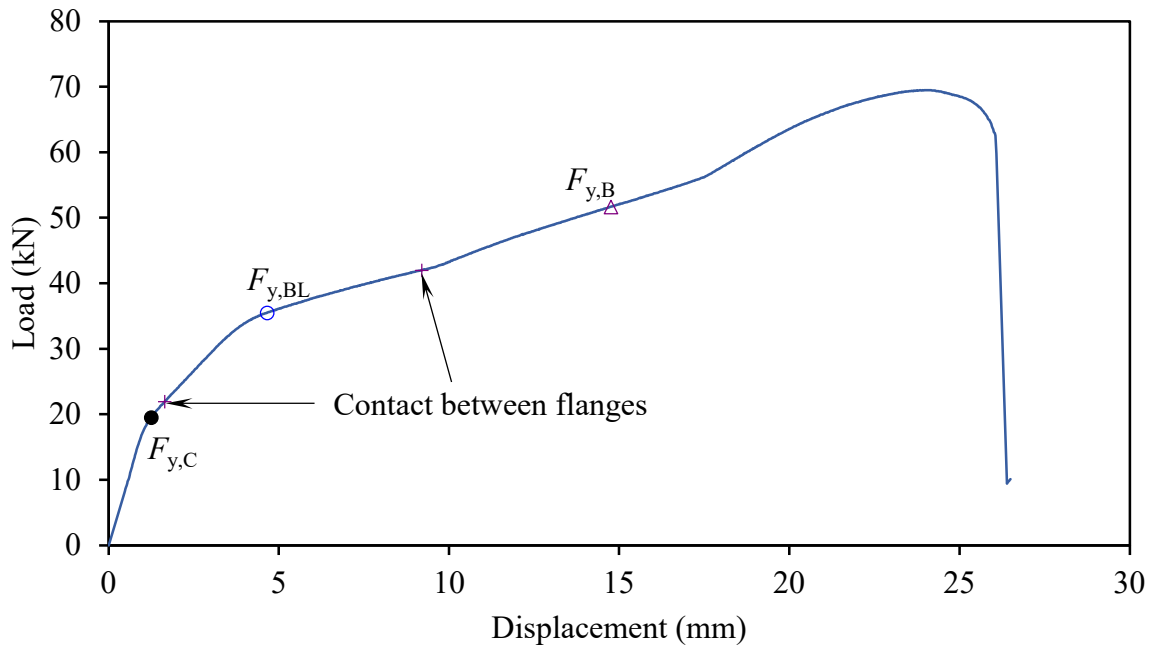
(a) Two-stage behaviour – Mode 2
(Specimen T1-40-2.00-C-R)



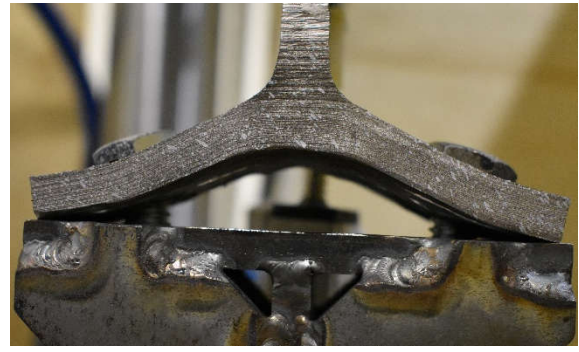
(b) Two-stage behaviour with an additional kink – Mode 2
(Specimen T1-70-0.67-C-S)



(c) Two-stage behaviour with two additional kinks – Mode 1
(Specimen T1-160-1.50-C-S)



(d) Three-stage behaviour with an additional kink – Mode 1
(Specimen T1-60-0.40-C-S)



(a) Specimens T1-40-0.67-C-S (top) and T1-40-2.00-C-S (bottom)

(b) Specimens T1-40-0.67-C-R (top) and T1-60-0.67-I-R (bottom)

Figure 17. Typical specimens failing in (a) Mode 1 and (b) Mode 2

58
59
60
61
62
63
64
65
66
67



(a) Ultimate bolt failures



(b) Shear-out failure
(Specimen T1-90-0.33-C-R)



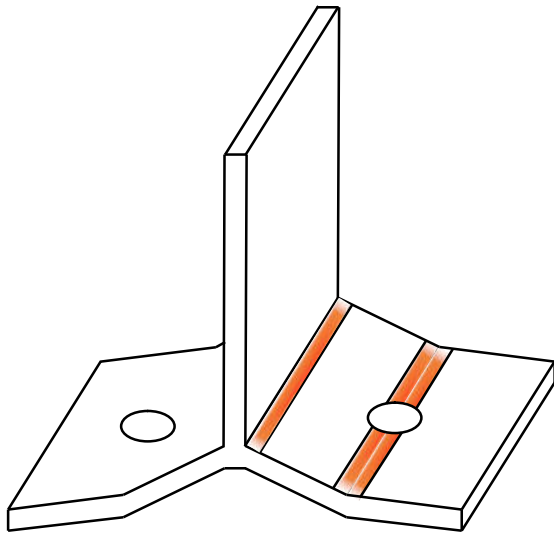
(c) Punching failure (Specimen T2-140-1.83-C-R)

Figure 18. Ultimate failure of tested T-stubs

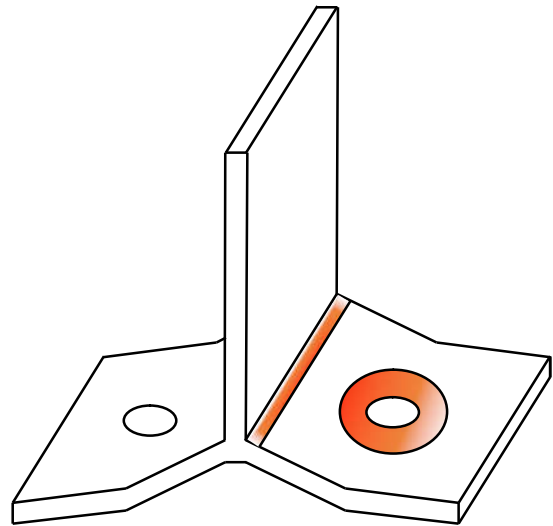
68

69

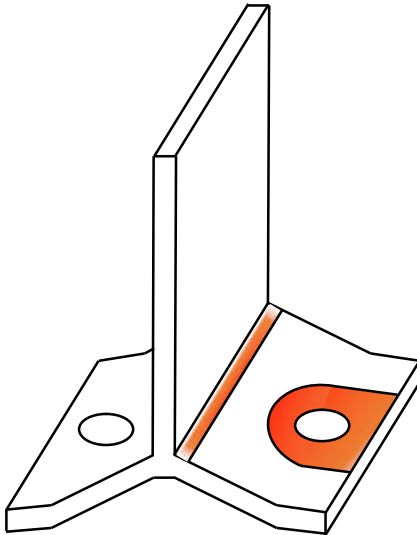
70



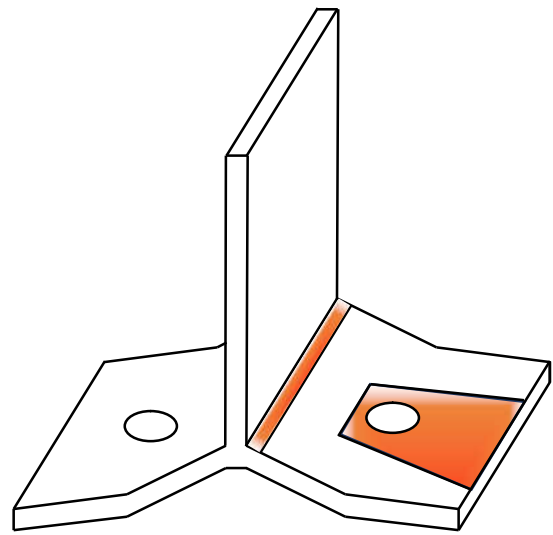
(a) Beam pattern



(b) Circular pattern (full circle)



(c) Circular pattern (circular individual end)

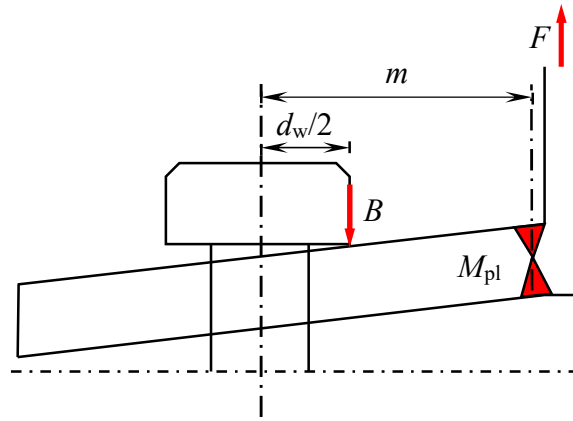


(d) Non-circular

71 **Figure 19.** Theoretical yield line patterns: (a) beam, (b) circular with full circle, (c) circular
72 individual end and (d) non-circular

73

74



75

76

Figure 20. Improved model recognising the influence of the bolt head size

77

F = applied load, B = force at the bolt head.

78

79

80

81

82

83

84

85

86

87

88